A Decentralised Neural Model Explaining Optimal Integration of Navigational Strategies in Insects

Xuelong Sun[1], **Shigang Yue**[1,3†], **Michael Mangan**[2†]

***For correspondence:**
syue@lincoln.ac.uk;
m.mangan@sheffield.ac.uk;
xsun@lincoln.ac.uk

[†]Joint last authorship

[1]Computational Intelligence Lab & L-CAS, School of Computer Science, University of Lincoln, United Kingdom; [2]Sheffield Robotics, Department of Computer Science, University of Sheffield, Sheffield, United Kingdom; [3]Machine Life and Intelligence Research Centre, Guangzhou University, China

Abstract

Insect navigation arises from the coordinated action of concurrent guidance systems but the neural mechanisms through which each functions, and are then coordinated, remains unknown. We propose that insects require distinct strategies to retrace familiar routes (route-following) and directly return from novel to familiar terrain (homing) using different aspects of frequency encoded views that are processed in different neural pathways. We also demonstrate how the Central Complex and Mushroom Bodies regions of the insect brain may work in tandem to coordinate the directional output of different guidance cues through a contextually switched ring-attractor inspired by neural recordings. The resultant unified model of insect navigation reproduces behavioural data from a series of cue conflict experiments in realistic animal environments and offers testable hypotheses of where and how insects process visual cues, utilise the different information that they provide and coordinate their outputs to achieve the adaptive behaviours observed in the wild.

Introduction

Central-place foraging insects navigate using a 'toolkit' of independent guidance systems (***Wehner, 2009***) of which the most fundamental are path integration (PI), whereby foragers track the distance and direction to their nest by integrating the series of directions and distances travelled (for reviews see ***Heinze et al.*** (***2018***); ***Collett*** (***2019***)), and visual memory (VM), whereby foragers derive a homing signal by comparing the difference between current and stored views (for reviews see ***Zeil*** (***2012***); ***Collett et al.*** (***2013***)). Neurophysiological and computational modelling studies advocate the central complex neuropil (CX) as the PI centre (***Heinze and Homberg, 2007***; ***Seelig and Jayaraman, 2015***; ***Stone et al., 2017***), whereas the mushroom body neuropils (MB) appear well suited to assessing visual valence as needed for VM (***Heisenberg, 2003***; ***Ardin et al., 2016***; ***Müller et al., 2018***). Yet, two key gaps in our understanding remain. Firstly, although current VM models based on the MB architecture can replicate route following (RF) behaviours whereby insects visually recognise the direction previously travelled at the same position previously (***Ardin et al., 2016***; ***Müller et al., 2018***), they cannot account for visual homing (VH) behaviours whereby insects return directly to their familiar surroundings from novel locations following a displacement (e.g. after being blown off course by a gust of wind) (***Wystrach et al., 2012***). Secondly, despite increasing neuroanatomical evidence suggesting that premotor regions of the CX coordinate navigation behaviour (***Pfeiffer***

and Homberg, 2014; *Heinze and Pfeiffer, 2018*; *Honkanen et al., 2019*), a theoretical hypothesis explaining how this is achieved by the neural circuitry has yet to be developed. In this work we present a unified neural navigation model that extents the core guidance modules from two (PI and VM) to three (PI, RF, and VH) and by integrating their outputs optimally using a biologically realistic ring attractor network in the CX produces realistic homing behaviours.

The foremost challenge in realising this goal is to ensure that the core guidance subsystems provide sufficient directional information across conditions. Contemporary VM models based on the MBs can replicate realistic RF behaviours in complex visual environments (ant environments: *Kodzhabashev and Mangan* (*2015*); *Ardin et al.* (*2016*), bee environments: *Müller et al.* (*2018*)) but do not generalise to visual homing scenarios whereby the animal must return directly to familiar terrain from novel locations (ants: *Narendra* (*2007*), bees: *Cartwright and Collett* (*1982*), wasps: *Stürzl et al.* (*2016*)). Storing multiple nest-facing views before foraging, inspired by observed learning walks in ants (*Müller and Wehner, 2010*; *Fleischmann et al., 2016*) and flights in bees and wasps (*Zeil et al., 1996*; *Zeil and Fleischmann, 2019*), provides a potential solution (*Graham et al., 2010*; *Wystrach et al., 2013*), but simulation studies have found this approach to be brittle due to high probabilities of aligning with the wrong memory causing catastrophic errors (*Dewar et al., 2014*). Moreover, ants released perpendicularly to their familiar route do not generally align with their familiar visual direction as predicted by the above algorithms (*Wystrach et al., 2012*), but instead move directly back towards the route (*Fukushi and Wehner, 2004*; *Kohler and Wehner, 2005*; *Narendra, 2007*; *Mangan and Webb, 2012*; *Wystrach et al., 2012*), which would require a multi-stage mental alignment of views for current models. New computational hypothesis are thus required that can guide insects directly back to their route (often moving perpendicularly to the habitual path), but also allow for the route direction to be recovered (now aligned with the habitual path) upon arrival at familiar surroundings (see *Figure 1*A "Zero Vector").

With the necessary elemental guidance systems defined, a unifying model must then convert the various directional recommendations into a single motor command appropriate to the context (*Cruse and Wehner, 2011*; *Hoinville et al., 2012*; *Collett et al., 2013*; *Webb, 2019*). Behavioural studies show that when in unfamiliar visual surroundings ("Off-Route") insects combine the outputs of their PI and VH systems (*Collett, 1996*; *Bregy et al., 2008*; *Collett, 2012*) relative to their respective certainties consistent with optimal integration theory (*Legge et al., 2014*; *Wystrach et al., 2015*) (*Figure 1*A "Full Vector"). Upon encountering their familiar route, insects readily recognise their surroundings, recover their previous bearing and retrace their familiar path home (*Harrison et al., 1989*; *Kohler and Wehner, 2005*; *Wystrach et al., 2011*; *Mangan and Webb, 2012*). Thus, the navigation coordination model must posses two capabilities: (a) output a directional signal consistent with the optimal integration of PI and VH when Off-Route (b) switch from Off-Route (PI and VH) to On-Route (RF) strategies when familiar terrain is encountered. Mathematical models have been developed that reproduce aspects of cue integration in specific scenarios (*Cruse and Wehner, 2011*; *Hoinville and Wehner, 2018*), but to date no neurobiologically constrained network revealing how insects might realise these capabilities has been developed.

To address these questions a functional modelling approach is followed that extends the current base model described by *Webb* (*2019*) to (a) account for the ability of ants to home from novel locations back to the familiar route before retracing their familiar path the rest of the journey home, and (b) propose a neurally-based model of the central complex neuropil that integrates competing cues optimally and generates a simple steering command that can drive behaviour directly. Performance is bench-marked by direct comparison to behavioural data reported by *Wystrach et al.* (*2012*) (showing different navigation behaviours on and off the route), *Legge et al.* (*2014*); *Wystrach et al.* (*2015*) (demonstrating optimal integration of PI and VM), and through qualitative comparison to extended homing paths where insects switch between strategies according to the context (*Narendra, 2007*). Biological realism is enforced by constraining models to the known anatomy of specific brain areas, but where no data exists an exploratory approach is taken to investigate the mechanisms that insects may exploit. *Figure 1*A depicts the adaptive behaviours observed in

animals that we wish to replicate accompanied by a functional overview of our unified model of insect navigation (***Figure 1***B) mapped to specific neural sites (***Figure 1***C).

Results

Mushroom bodies as drivers of rotational invariant visual homing

For ants to return directly to their familiar route after a sideways displacement (***Figure 1***A "Zero Vector") without continuous mental or physical realignment they require access to rotational invariant visual cues. ***Stone et al.*** (***2018***) recently demonstrated that binary images of panoramic skylines converted into their frequency components can provide such a rotationally-invariant encoding of scenes in a compact form (see Image processing for an introduction to frequency transformations of images). Moreover, they demonstrated that the difference between the rotationally invariant features (the **amplitudes** of the frequency coefficients) between two locations increases monotonically with distance producing an error surface reminiscent of the image difference surfaces reported by ***Zeil et al.*** (***2003***) which can guide an agent back to familiar terrain. Here we investigate whether the MB neuropils shown capable of assessing the visual valence of learned rotationally-varying panoramic skylines for RF (***Ardin et al., 2016***; ***Müller et al., 2018***), might instead assess the visual valence of rotationally-invariant properties of views sampled along a familiar route supporting visual homing.

To this end, the intensity sensitive input neurons of ***Ardin et al.*** (***2016***)'s MB model are replaced with input neurons encoding rotational invariant **amplitudes** (***Figure 2***A left, blue panel). The network is trained along an $11m$ curved route in a simulated world that mimics the training regime of ants in ***Wystrach et al.*** (***2012***) (see Methods and Materials and Reproduce visual navigation behaviour for details on simulated world, image processing, model architecture and training and test regime). After training, the firing rate of the MB output neuron (MBON) when placed at locations across the environment at random orientations reveals a gradient that increases monotonically with distance from the familiar route area, providing a homing signal sufficient for VH independent of the animal's orientation (***Figure 2***C).

Motor output is generated by connecting the MBON to the recently discovered CX steering network (***Stone et al., 2017***; ***Honkanen et al., 2019***). The CX steering circuit, proposed to reside in the fan-shaped body (FB/CBU), was proposed by ***Stone et al.*** (***2017***) to decrease the offset between the animal's current heading (a simulated celestial compass) and the desired heading (PI home vector). Their key insight was that the anatomically observed shift of activity in the columnar neurons that encode the desired heading in essence simulate 45° turns left and right allowing evaluation of the best direction to turn. ***Figure 2***A provides an example of this computation using the identified neural rings with the current heading defined by the global compass cells (green) with peak activity to the right, and the desired heading cells (red) having a peak pointing straight ahead. CPU1 cells (blue) evaluating the utility of a left turn then sum the difference in activity between the current heading and a 45° leftward shifted direction from the desired heading which generates a strong response as there is little overlap in the activity of these rings. In contrast, the CPU1 cells (blue) evaluating the utility of a right turn sum the difference in activity between the current heading and a 45° right shifted direction which produces a weak response as current and desired headings strongly overlap and thus largely cancel out. Taken together the animal would steer to the left which would decrease the mismatch between current and desired headings. The vector abstraction of this computation is also shown in ***Figure 2***A.

In the proposed VH model the current heading input to the steering circuit is derived from the same simulated global compass following a sinusoidal activity profile in a ring of l-TB1 neurons found in the protocerebral bridge (PCB/PB) (***Figure 2***A green ring). A desired heading is then generated by copying the current activity pattern of the global compass neurons to a new neural ring which we speculate could reside in either a distinct subset of l-TB1 neurons (***Beetz et al., 2015***) or in the FB. Crucially, the copied activity profile also undergoes a leftward shift proportional to

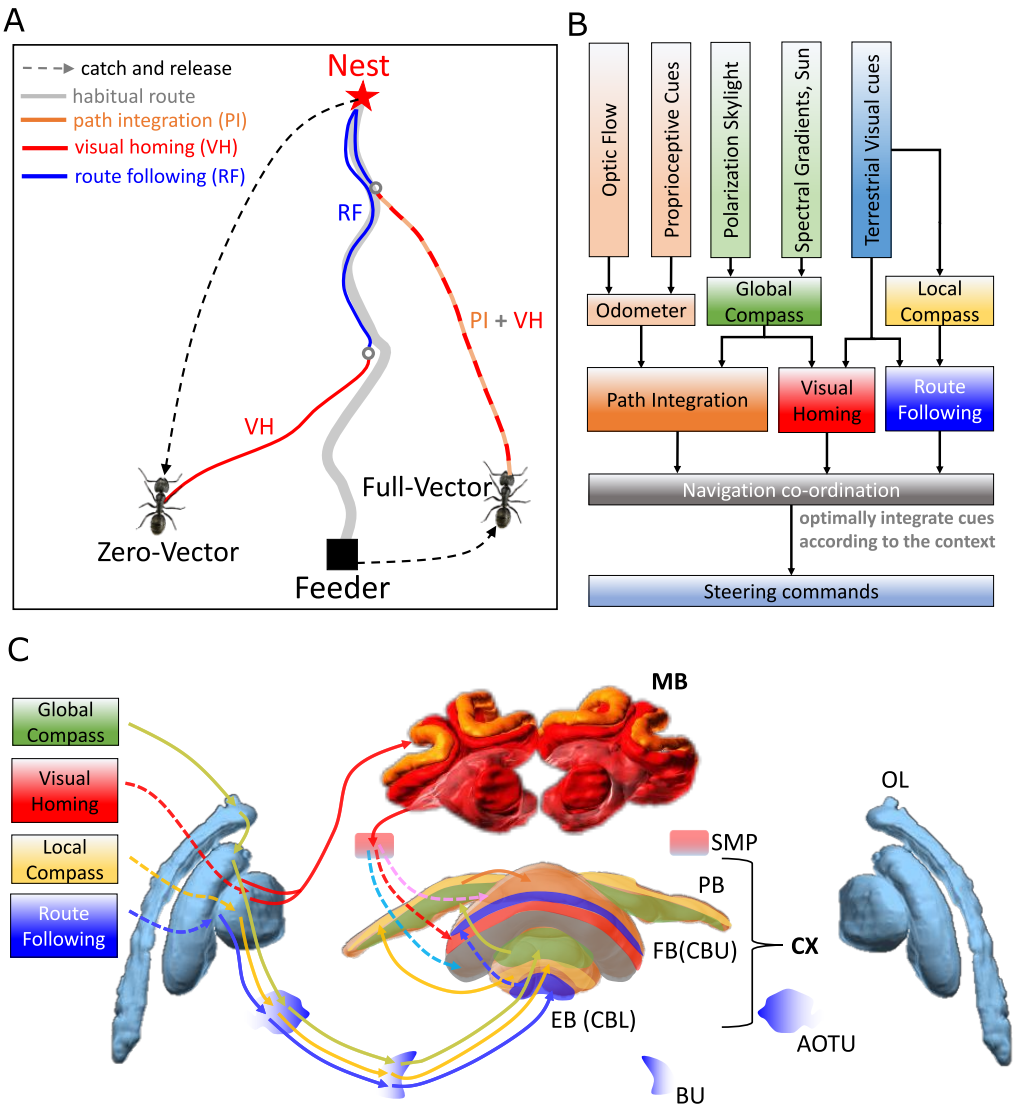

Figure 1. Overview of the unified navigation model and it's homing capabilities. (**A**) The homing behaviours to be produced by the model when displaced either from the nest and having no remaining PI home vector (zero vector), or from the nest with a full home vector (full vector). Distinct elemental behaviours are distinguished by coloured path segments, and stripped bands indicate periods where behavioural data suggests that multiple strategies are combined. Note that this colour coding of behaviour is maintained throughout the remaining figures to help the reader map function to brain region. (**B**) The proposed conceptual model of the insect navigation toolkit from sensory input to motor output. Three elemental guidance system are all modelled in this paper: path integration (PI), visual homing (VH) and route following (RF). Their outputs must then be coordinated in an optimal manner appropriate to the context before finally outputting steering command. (**C**) The unified navigation model maps the elemental guidance systems to distinct processing pathways: ***RF***: OL -> AOTU -> BU -> CX; ***VH***: OL -> MB -> SMP -> CX; ***PI***: OL -> AOTU -> BU -> CX. The outputs are then optimally integrated in the proposed ring attractor networks of the FB in CX to generate a single motor steering command. Connections are shown only for the left brain hemisphere for ease of visualisation but in practice are mirrored on both hemispheres. Hypothesised or assumed pathways are indicated by dashed lines whereas neuroanatomically supported pathways are shown by solid lines (a convention maintained throughout all figures).
OL: optic lobe, *AOTU*: anterior optic tubercle, *CX*: central complex, *PB*: protocerebrum bridge, *FB*: fan-shape body (or *CBU*: central body upper), *EB*: ellipsoid body (or *CBL*: central body lower), *MB*: mushroom body, *SMP*: superior medial protocerebrum, *BU*: bulb.
Images of the brain regions are adapted from the insect brain database https://www.insectbraindb.org.

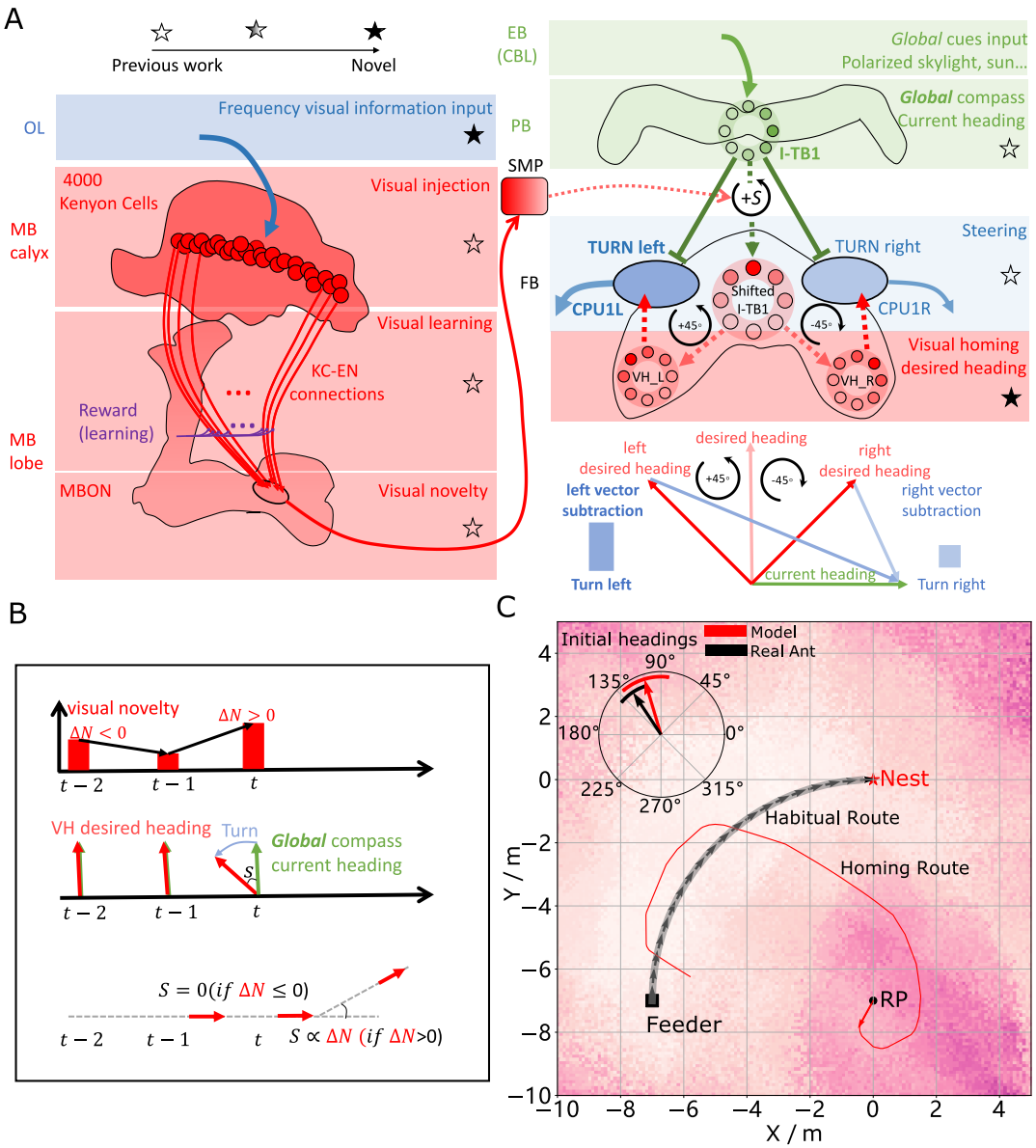

Figure 2. Visual Homing in the Insect Brain. (**A**) Neural model of visual homing. Rotational-invariant **amplitudes** are input to the MB calyx which are then projected to the Kenyon cells (KCs) before convergence onto the MB output neuron (MBON) which seeks to memorise the presented data via reinforcement learning based plasticity (more details see Visual homing) (MB circuit: left panels). SMP neurons measure positive increases in visual novelty (through input from the MBON) which causes a shift between the current heading (green cells) and desired headings (red cells) in the rings of the CX (SMP pathway between MB and CX: centre panel; CX circuit: right panels). The CX-based steering circuit then computes the relevant turning angle. Each model component in all figures is labelled with a shaded star to indicate what aspects are new versus those incorporated from previous models (see legend in upper left). (**B**) Time series of the proposed visual homing model. When visual novelty drops ($t-2$ to $t-1$) the desired heading is an unshifted copy of the current heading so the current path is maintained but when the visual novelty increases ($t-1$ to t) the desired heading is shifted from the current heading and the agent changes direction. (**C**) The firing rate of the MBON sampled across locations at random orientations is depicted by the heat-map showing a clear gradient leading back to the route. The grey curve shows the habitual route along which ants were trained. RP (release point) indicates the position where real ants in ***Wystrach et al.*** (***2012***) were released after capture at the nest (thus zero-vector) and from which simulations were started. The ability of the VH model to generate realistic homing data is shown by the initial paths of simulated ants which closely match those of real ants (see inserted polar plot showing the mean direction and 95% confidential interval), and also the extended exampled path shown (red line). Note that once the agent arrives in the vicinity of the route, it appears to meander due the flattening of visual novelty gradient and the lack of directional information.

Figure 2–source data 1. The frequency information for the locations with random orientations across the world.

Figure 2–source data 2. The visual homing results of the model

any increase in visual novelty which we propose is measured by neurons in the superior medial protocerebrum (SMP) (***Aso et al., 2014***; ***Plath et al., 2017***) (see ***Figure 2***A centre and activity of red rings). Note that we use the term ring network to describe a group of neurons whose pattern of activity forms a circular representation regardless of actual physical arrangement which we differentiate from ring attractor networks introduced later. The result is a mechanism that recommends changing direction when the agent moves away from familiar terrain (visual novelty increases) but recommends little change to the current heading when the visual novelty is decreasing. Thus, the model iteratively refines it's orientation to descend the visual novelty gradient and thus recover familiar terrain (***Figure 2***B).

Figure 2C demonstrates that the proposed network accurately replicates both the directed initial paths as in ***Wystrach et al.*** (***2012***) (see the inserted black arrow), and extended homing paths as in ***Narendra*** (***2007***) observed in ants displaced to novel locations perpendicular to their familiar routes. We note that upon encountering the route the model is unable to distinguish the direction in which to travel and thus meanders back and forth along the familiarity valley, unlike real ants, demonstrating the need for additional route recognition and recovery capabilities.

Optimally integrating visual homing and path integration

We have demonstrated how ants could use visual cues to return to the route in the absence of PI but in most natural scenarios (e.g. displacement by a gust of wind) ants will retain a home vector readout offering an alternative, and often conflicting, guidance cue to that provided by VH. In such scenarios desert ants strike a comprise by integrating their PI and VH outputs in a manner consistent with optimal integration theory by weighting VH relative to the familiarity of the current view (***Legge et al., 2014***) and PI relative to the home vector length (a proxy for directional certainty) (***Wystrach et al., 2015***).

Artificial ring-attractor networks, similar to those found in the CX (***Green et al., 2017***), output the weighted sum of their inputs approximating optimal cue integration (***Touretzky, 2005***; ***Sun et al., 2018***) offering a biologically realistic means to weight PI and VH cues. Thus a pair of ring-attractor networks are added to the CX model (***Figure 3***A grey neural rings: RA_L and RA_R) that take as input the desired headings from the above proposed VH model (red neural rings: VH_L and VH_R) and ***Stone et al.*** (***2017***)'s PI model (orange neural rings: PI_L and PI_R) and output combined Off Route desired heading signals that are sent to the steering circuits (blue neural rings: CPU_L and CPU_R). ***Stone et al.*** (***2017***) mapped the home vector computation to a population of neurons (CPU4) owing to their dual inputs from direction selective compass neurons (I_TB1) and motion sensitive speed neurons (TN2) as well as their recurrent connectivity patterns facilitating accumulation of activity as the animal moves in a given direction. ***Wystrach et al.*** (***2015***) showed that the certainty of PI automatically scales with the home-vector length owing to the accumulating effect of the memory neurons which correlates with directional uncertainty, and thus the output PI network is directly input to the ring attractor circuits. In our implementation the VH input has a fixed height and width profile and influences the integration through tuning neurons (TUN) (see the plotted activation function in ***Figure 3***B and Optimal cue integration) that we suggest reside in the SMP and modulate the PI input to the integration network. Altering the weighting in the this manner rather than by scaling the VH input independently allows VH to dominate the integrated output at sites with high visual familiarity even in the presence of a large home vector without having large stored activity. We note however, that both approaches remain feasible and further neuroanatomical data is required to clarify which, if either, mechanism is employed by insects.

Figure 3C shows the initial headings produced by the model which replicates the trends reported in cue-conflict experiments by ***Legge et al.*** (***2014***) and ***Wystrach et al.*** (***2015***) when the uncertainty of PI and VH cues were altered independently. Example extended paths of independent PI and VH models and the ring-attractor-based combined PI and VH model are plotted in ***Figure 3***D with the combined model showing the most ant-like behaviour (***Kohler and Wehner, 2005***; ***Mangan and Webb, 2012***) by initially following predominantly the home-vector direction before switching

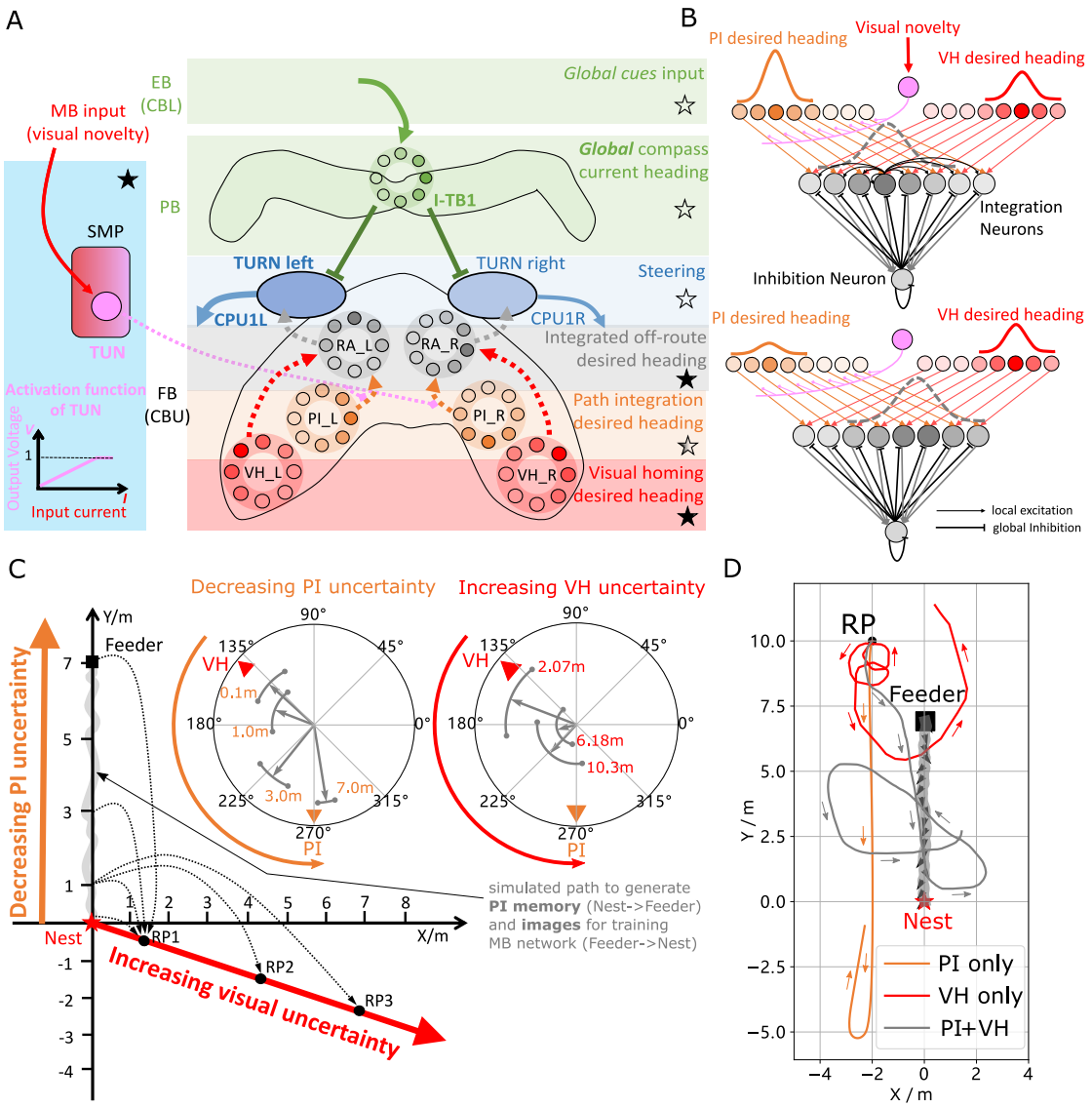

Figure 3. Optimal cue integration in the CX. (**A**) Proposed model for optimally integrating PI and VH guidance systems. In each hemisphere, ring attractors (RAs) (grey neural rings) receive the corresponding inputs from PI (orange neural rings) and VH (red neural rings) with the outputs sent to the corresponding steering circuits (blue neural rings). Integration is weighted by the visual novelty tracking tuning neuron (TUN) whose activation function is shown in the leftmost panel. (**B**) Examples of optimal integration of PI and VH headings for two PI states with the peak stable state (grey dotted activity profile in the integration neurons) shifting towards VH as the home vector length recedes. (**C**) Replication of optimal integration studies of ***Wystrach et al.*** (***2015***) and ***Legge et al.*** (***2014***). Simulated ants are captured at various points (0.1m, 1m, 3m and 7m) along their familiar route (grey curve) and released at release point 1 (RP1) thus with the same visual certainty but with different PI certainties as in ***Wystrach et al.*** (***2015***) (see thick orange arrow). The left polar plot shows the initial headings of simulated ants increasingly weight their PI system (270°) in favour of their VH system (135°) as the home vector length increases and PI directional uncertainty drops. Simulated ants are also transferred from a single point 1m along their familiar route to ever distant release points (RP1, RP2, RP3) thus with the same PI certainty but increasingly visual uncertainty as in ***Legge et al.*** (***2014***) (see thick red arrow). The right polar plot shows the initial headings of simulated ants increasingly weight PI (270°) over VH (135°) as visual certainty drops. (see Reproduce the optimal cue integration behaviour for details) (**D**) Example homing paths of the independent and combined guidance systems displaced from the familiar route (grey) to a fictive release point (RP)

Figure 3–Figure supplement 1. The extended homing paths and the PI memory in the simulations

Figure 3–source data 1. The results of tuning PI uncertainty.

Figure 3–source data 2. The results of tuning VH uncertainty.

Figure 3–source data 3. The extended homing path of PI, VH and combined PI and VH.

to visual homing when the home-vector length drops leading the simulated ant back to familiar terrain. Note that the PI-only and PI+VH models are drawn back towards their fictive nest sites indicated by their home vectors which if left to run would likely resulted in emergent search-like patterns as in ***Stone et al.*** (***2017***). Moreover, upon encountering the route the VH-based models (VH-only and PI+VH) are unable to distinguish the direction in which to travel and hence again (see meander around the valley of familiarity ***Figure 2***C) further demonstrating a need for a route recovery mechanism.

Route following in the insect brain

The model described above can guide insects back to their familiar route area, but lacks the means to recover the route direction upon arrival as observed in homing insects. This is not surprisingly as VH relies upon translationally-varying but rotational-invariant information whereas RF requires rotationally-varying cues. Thus we introduce a new elemental guidance system that makes use of the rotationally-varying *phase* coefficients of the frequency information derived from the panoramic skyline which tracks the orientation of specific features of the visual surroundings (see Methods and Materials). Here we ask whether by associating the rotationally invariant **amplitudes** (shown useful for place recognition) with the rotationally-varying *phases* experienced at those locations, insects might recover the familiar route direction.

Neuroanatomical data with which to constrain a model remains sparse and therefore a standard artificial neural network (ANN) architecture is used to investigate the utility of *phase*-based route recovery with biological plausibility discussed in more detail below. A 3-layer ANN was trained to associate the same 81 rotational-invariant **amplitudes** as used in the VH model with the rotational varying *phase* value of single frequency coefficient experienced when travelling along the habitual route which we encode in an 8 neuron-ring (see ***Figure 4***A and Route Following for detailed model description). Thus, when the route is revisited the network should output the orientation that the *phase* converged upon when at the same location previously, which we note is not necessarily aligned with the actual heading of the animal (e.g. it may track the orientation to vertical bar (***Seelig and Jayaraman, 2015***)). Realignment is possible using the same steering mechanism as described above but which seeks to reduce the offset between the current *phase* readout (e.g. a local compass locked onto visual features of the animals surroundings), and the recalled *phase* readout from the ANN.

We speculate that the most likely neural pathways for the new desired and current headings are from Optic Lobe via Anterior Optic Tubercle (AOTU) and Bulb to EB (CBL) of the CX (***Homberg et al., 2003***; ***Beetz et al., 2015***) (see ***Figure 4***A) with the desired heading terminating in the EB whereas the current heading continues to the PB forming a local compass that sits beside the global compass used by PI and VH systems. That's to say that, firstly, there are two parallel pathways forming two compass systems- the global (here based on celestial cues) and the local (based on terrestrial cues) compasses modelled by the activation of I-TB1 and II-TB1 neurons respectively. The four classes of CL1 neurons (or E-PG and P-EG neurons) found described by ***Heinze and Homberg*** (***2009***); ***Xu et al.*** (***2020***) and the independent TB1 neurons found outlined in ***Beetz et al.*** (***2015***) provide the potential for two parallel recurrent loops encoding independent local and global compasses. Secondly, the desired heading, which is the recalled *phase* of a specific view, is generated through the neural plasticity from AOTU to BU and BU to EB, which is line with recent evidence of associative learning between the R-neurons transmitting visual information from BU to EB and the compass neurons (CL1a or E-PG neurons) that receive input from EB (***Kim et al., 2019***; ***Fisher et al., 2019***). This kind of learning endows the animal with the ability to flexibly adapt their local compass and also desired navigational orientation according to the changing visual surroundings. The use of the same steering circuit is also feasible by comparison of the local compass activity (II-TB1) with the desired heading via a direct link between EB to FB neurons (***Hausen and Egelhaaf, 1989***).

The RF model accurately recovers the initial route heading in a similar manner to real ants returned to the start of their familiar route (***Wystrach et al., 2012***) (***Figure 4***B, insert), and then follows

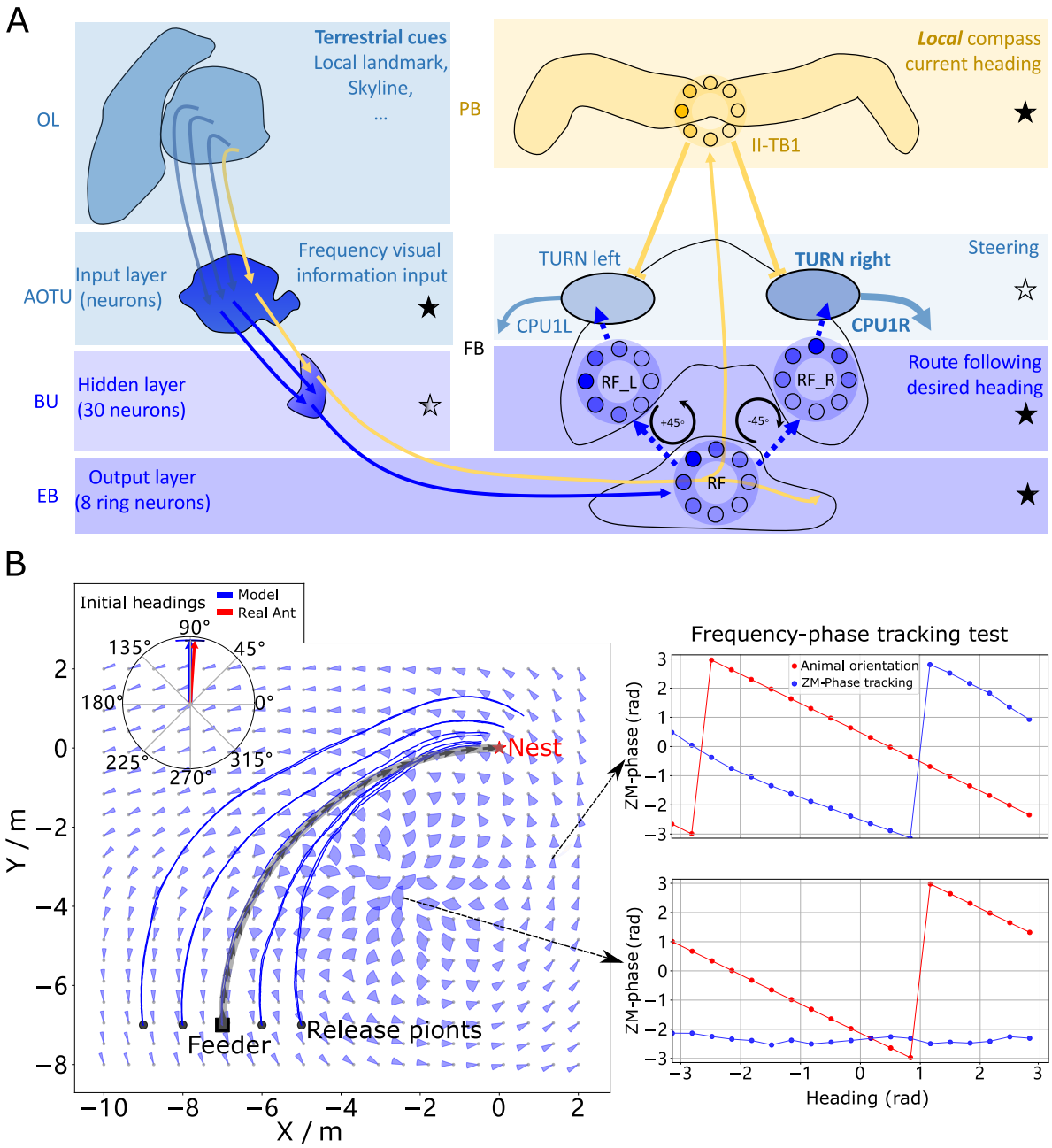

Figure 4. Phase-based route following. (**A**) Neural model. The visual pathway from the optic lobe via AOTU and Bulb to EB of the CX is modelled by a fully connected artificial neural network (ANN) with one hidden layer. The input layer receives the **amplitudes** of the frequency encoded views (as for the MB network) and the output layer is an 8-neuron ring whose population encoding represents the desired heading against to which the agent should align. (**B**) Behaviours. Blue and red arrows in the inserted polar plot (top left) display the mean directions and 95% confidential intervals of the initial headings of real (***Wystrach et al., 2012***) and simulated ants released at the start of the route $(-7, -7)$ respectively. Dark blue curves show the routes followed by the model when released at 5 locations close to the start of the learned path. The overlaid fan-plots indicate the circular statistics (the mean direction and 95% confidential interval) of the homing directions recommended by the model when sampled across heading directions (20 samples at 18°intervals). Data for entire rotations are shown on the right for specific locations with the upper plot, sampled at $(1.5, -3)$, demonstrating accurate phase-based tracking of orientation, whereas the lower plot sampled at $(-2.5, -3.5)$ shows poor tracking performance and hence produces a wide fan-plot.

Figure 4–source data 1. The frequency tracking performance across the world.

Figure 4–source data 2. The RF model results of the agents released on route.

Figure 4–source data 3. The RF model results of the agents released aside from the route.

the remaining route in its entirety back to the nest again reflecting ant data (***Kohler and Wehner, 2005***; ***Mangan and Webb, 2012***) (***Figure 4***B). The quiver plots displayed in the background of ***Figure 4***B show the preferred homing direction output by the ANN when rotated on the spot across locations in the environment. The noise in the results are due to errors in the tracking performance (see examples ***Figure 4***B right) yet as these errors are in largely confined to the magnitude, the steering circuit still drives the ant along the route. We note that this effect is primarily a function of the specific frequency transformation algorithm used which we borrow from computer graphics to investigate the utility of frequency encoding of visual information. The biological realism of such transforms and their potential implementation in the insect vision system are addressed in the Discussion. The displaced routes also highlight the danger of employing solely RF which often shadows rather than converges with the route when displaced sideways, further demonstrating the necessity for integration with the Off-Route strategies that promote route convergence.

Route recovery through context-dependent modulation of guidance systems

Homing insects readily recognise familiar route surroundings, recover their bearing, and retrace their habitual path home, irrespective of the status of other guidance system such as PI. Replicating such context-dependent behavioural switching under realistic conditions is the final task for the proposed model. The visual novelty measured by the MBON provides an ideal signal for context switching with low output when close to the route when RF should dominate versus high output further away from the route when PI and VH should be engaged (see ***Figure 2***C). Also the fact that Off-route strategies (PI and VH) compute their turning angles with reference to the global compass whereas the On-route RF strategy is driven with reference to a local compass provides a means to modulate their inputs to the steering circuit independently. This is realised through a non-linear weighting of the On and Off-route strategies which we propose acts through the same SMP pathway as the VH model (see the SN1 and SN2 neurons in ***Figure 5***A) (see Context-dependent switch for neuron details and ***Figure 7*** for a force-directed graph representation of the final unified model).

The activity of the proposed switching circuit and the paths that it generates in simulated zero vector and full vector displacement trials are shown in ***Figure 5*** B & C respectively. In the full vector trial (***Figure 5***B (upper), ***Figure 5***C (solid line)) as visual novelty is initially high (see high TUN activity until step 78) SN2 is activated which enables Off-Route strategies (PI and VH) while SN1 (always the inverse of SN2) is deactivated which disables On-Route strategies. Note that it is the integration of PI and VH that generates the direct path back to the route area in the FV trial: PI recommends moving at a 45° bearing but VH prevents ascension of the visual novelty gradient that this would cause with the compromise being a bearing closer to 90° i.e. toward the route. As the route is approached the visual novelty decreases (again see TUN activity), until at step 78 SN2 falls below threshold and deactivates the Off-Route strategies while conversely SN1 activates and engages On-Route strategies. After some initial flip-flopping while the agents converges on the route (steps 78-85) RF becomes dominant and drives the agent back to the nest via the familiar path. In the zero vector trial (***Figure 5***B (lower), (***Figure 5***B (dashed line)) Off-route strategies (here only VH) largely dominate (some false positive route recognition (e.g step 60)) until the route is recovered (step 93), at which point the same flip-flopping during route convergence occurs (steps 93-96) followed by RF alone which returns the agent to the nest via the familiar path. It should be noted that the data presented utilised different activation functions of the TUN neuron that weights PI and VH (see ***Table 2*** for parameter settings across trials and Discussion for insights into model limitations and potential extensions), yet the results presented nevertheless provide a proof-of-principle demonstration that the proposed unified navigation model can fulfil all of the criteria defined for replication of key adaptive behaviour observed in insects (***Figure 1***A).

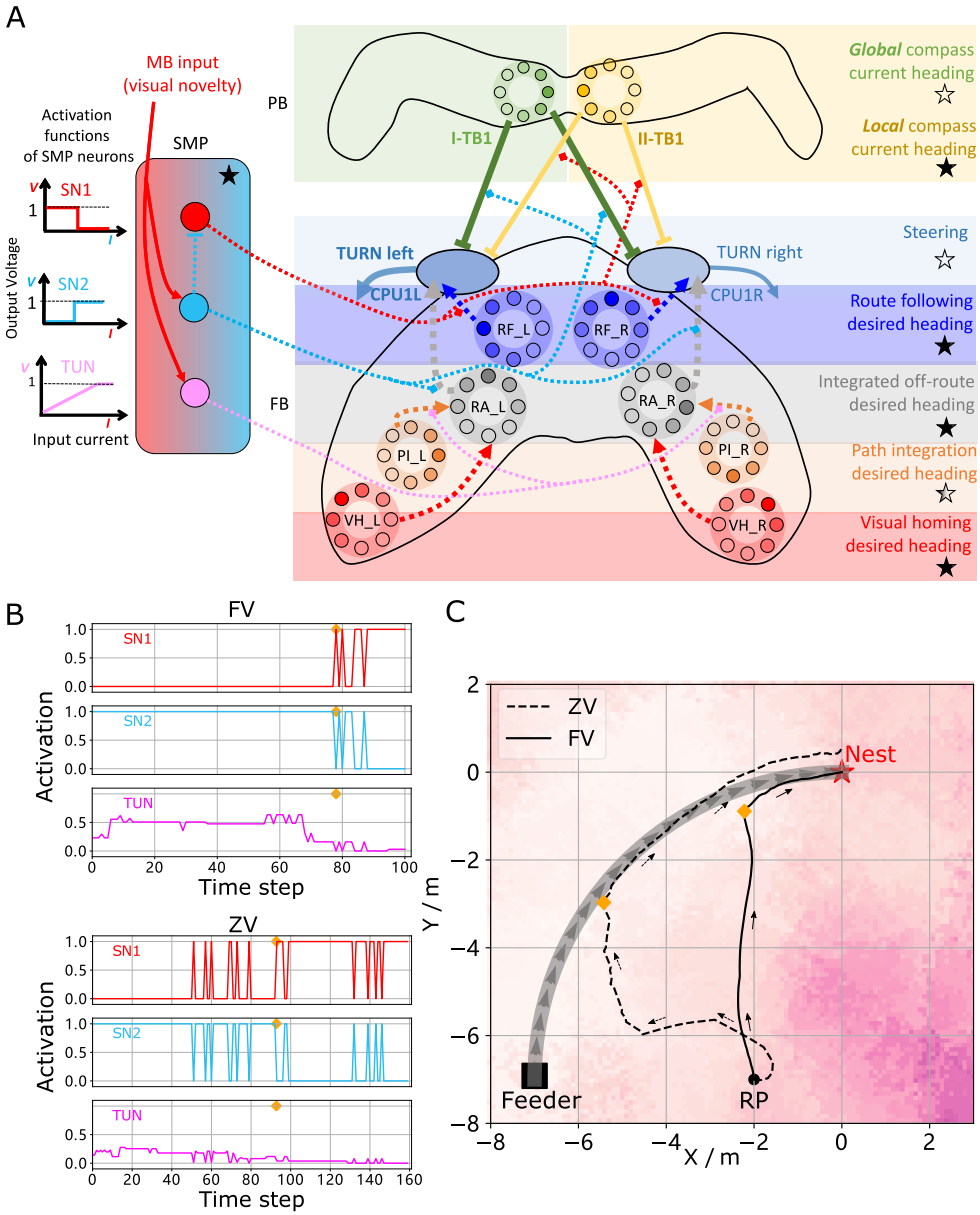

Figure 5. Unified model realising the full array of coordinated navigational behaviours. (**A**) Context-dependent switching is realised using two switching neurons (SN1, SN2) that have mutually exclusive firing states (one active while the other is in active) allowing coordination between On and Off-Route strategies driven by the instantaneous visual novelty output by the MB. Connectivity and activation functions of the SMP neurons are shown in the left side of panel. (**B**) Activation history of the SN1, SN2 and TUN (to demonstrate the instantaneous visual novelty readout of the MB) neurons during the simulated displacement trials. (**C**) Paths generated by the unified model under control of the context-dependent switch circuit during simulated FV (solid line) and ZV (dashed line) displacement trials.

Figure 5–source data 1. The navigation results of the whole model.

Discussion

This work addresses two gaps in the current understanding of insect navigation: what are the core visual guidance systems required by the insect navigational toolkit? And how are they coordinated by the insect brain?

We propose that the insect navigation toolkit (***Wehner, 2009***; ***Webb, 2019***) should be extended to include independent visual homing (VH) and route following (RF) systems (see ***Figure 1***B for

updated Insect Navigation Toolkit). We show how VH and RF can be realised using frequency-encoding of panoramic skylines to separate information into rotationally-invariant **amplitudes** for VH and rotationally-varying *phases* for RF. The current model utilises frequency encoding schema from the computer graphics but behavioural studies support the use of spatial frequency by bees (***Horridge, 1997***; ***Lehrer, 1999***), with neurons in the lobulla of dragonflies (***O'Carroll, 1993***) and locusts (***James and Osorio, 1996***) found to have receptive fields akin to basis functions, providing a mechanism by which to extract the frequency information necessary for the local compass system. Our model allows for this information extraction process to happen at multiple stage ahead of its usage in the central learning sites such as the MBs opening the possibility for its application in either the optic lobes or subsequent pathways through regions such as the AUTO. Further, neurophysiological data is required to pinpoint both the mechanisms and sites of this data processing in insects. Similarly, following ***Stone et al.*** (***2017***) the global compass signal directly mimics the firing pattern of compass neurons in the CX without reference to sensory input but ***Gkanias et al.*** (***2019***) recently presented a plausible neural model of the celestial compass processing pipeline that could be easily integrated into the current model to fill this gap. Follow-on neuroanatomically constrained modelling of the optic lobes presents the most obvious extension of this work allowing the neural pathway from sensory input to motor output signal to be understood with downstream extensions into motor generating mechanisms also possible (***Steinbeck et al., 2020***) to close the entire sensory-motor loop.

Visual homing is modelled on neural circuits found along the OL-MB-SMP pathway (***Ehmer and Gronenberg, 2002***; ***Gronenberg and López-Riquelme, 2004***) before terminating in the CX steering circuit (***Stone et al., 2017***) and shown capable of producing realistic homing paths. In this schema the MBs do not measure rotationally-varying sensory valence as recently used to replicate RF (***Ardin et al., 2016***; ***Müller et al., 2018***), but rather the spatially varying (but rotationally-invariant) sensory valence more suited to gradient descent strategies such as visual homing (***Zeil et al., 2003***; ***Stone et al., 2018***) and other taxis behaviours (***Wystrach et al., 2016***). This is inline with the hypothesis forwarded by ***Collett and Collett*** (***2018***) that suggest that the MBs output "whether" the current sensory stimulus is positive or negative and the CX then adapts the animal heading, the "whither", accordingly.

Route following is shown possible by learned associations between the **amplitudes** (i.e. the place) and the *phase* (the orientation) experienced along a route, allowing realignment when later at a proximal location. This kind of neural plasticity based correlation between the visual surroundings and the orientations fits with data recently observed in fruit flies (***Kim et al., 2019***; ***Fisher et al., 2019***). These studies provide the neural explanation for the animal's ability to make flexible use of visual information to navigation while the proposed model gives a detailed implementation of such ability in the context of insect's route following schema. Neurophysiological evidence suggests that the layered visual pathway from OL via AOTU and BU to the EB of the CX (***Barth and Heisenberg, 1997***; ***Homberg et al., 2003***; ***Omoto et al., 2017***) with its suggested neural plasticity properties (***Barth and Heisenberg, 1997***; ***Yilmaz et al., 2019***) provides a possible neural pathway but further analysis is needed to identify the circuit structures that might underpin the generation of RF desired heading. In addition to the desired heading, the current heading of RF is derived from the local compass system anchored to animal's immediate visual surroundings. This independent compass system may be realised parallel to the global compass system in an similar but independent ring attractor circuit (***Heinze and Homberg, 2009***; ***Beetz et al., 2015***; ***Xu et al., 2020***). Our model therefore hypothesises that insects possess different compass systems based on varied sensory information and further that insects possess the capability (via CX-based RAs) to coordinate their influence optimally according to the current context. Since the global compass, the local compass and the desired heading of RF share the same visual pathway (OL->AOTU->BU->CX), distinct input and output patterns along this pathway may be found by future neuroanatomical studies. In addition, in the proposed model, the activation of current heading and desired heading of RF overlap in the EB, and therefore separation of activation profiles representing each output (e.g. following

methods in ***Seelig and Jayaraman*** (***2015***)) presents another meaningful topic for future neurophysiological research.

Closed-loop behavioural studies during which the spatial frequency information of views is altered (similar to ***Paulk et al.*** (***2015***)) coincident with imaging of key brain areas (***Seelig and Jayaraman, 2013***, ***2015***) offers a means to investigate which neural structures make use of what visual information. Complimentary behavioural experiments could verify the distinct VH and RF systems by selectively blocking the proposed neural pathways with impacts on behaviour predicted by ***Figure 2***C and ***Figure 4***B respectively. ***Ofstad et al.*** (***2011***) report that visual homing abilities are lost for fruit flies with a blocked EB of the CX but not MB, which is predicted by our model if animals have learned target-facing views to which they can later align using their RF guidance system. Analysis of animal's orientation during learning is thus vital to unpicking precisely how the above results arise.

With the elemental guidance strategies defined, we propose that their outputs are coordinated through the combined action of the MBs and CX. Specifically, we demonstrate how ring attractor networks, following neural firing patterns recorded in the CX (***Green et al., 2017***), are sufficient for optimally weighting multiple directional cues from the same frame of reference (e.g. VH and PI). The optimal integration of PI and VH using a ring attractor closely matches the networks theorised to govern optimal directional integration in mammals (***Jeffery et al., 2016***) and supports hypothesis of their conserved use across animals (***Sun et al., 2018***). Optimality is secured either through adapting the shape of the activity profile of the input as is the case for PI which naturally scales with distance, or by using a standardised input activity profile with cross-inhibition of competing cues as is the case for VH in the model. The later schema avoids the need for ever increasing neural activity to maintain relevance.

While this assemblage recreates optimal integration of strategies that share a compass system, it does not easily extend to integration of directional cues from other frames of reference (e.g. VH and PI reference the global compass versus RF that references a local compass). Indeed as the CX steering network seeks to minimise the difference between a current and a desired heading, calibrating input signals from different frames of reference would require a similar calibration of their respective compass systems. Rather, the proposed model incorporates a context-dependent non-linear switching mechanism driven by the output of the MB that alternates between strategies: global compass based PI and VH are triggered when the surroundings are unfamiliar, but when in familiar surroundings engage local compass based RF. In summary, the adaptive behaviour demonstrated is the result of distinct guidance systems map that converge in the CX, with their relative weighting defined by the output of the MB. This distributed architecture is reminiscent of mechanisms found in the visual learning of honeybees (***Plath et al., 2017***), and supports the hypothesis that the CX is the navigation coordinator of insects (***Heinze, 2017***; ***Honkanen et al., 2019***) but shows how the MB acts as a mediator allowing the CX to generate optimal behaviour according to the context.

The resultant unified model of insect navigation ***Figure 1***B and C represents a proof-of-principle framework as to how insects might co-ordinate core navigational behaviours (PI, VH and RF) under standard field manipulations ***Figure 1***A. Neuroanatomical data has been drawn from across insect classes (see ***Table 1***) to ensure neural realism where possible with performance compared to ant navigation behaviour in a single simulated desert ant habitat. The framework can be easily extended to new navigation behaviours observed in other insects from idiothetic PI (***Kim and Dickinson, 2017***) to straight line following (***El Jundi et al., 2016***) to migrations (***Reppert et al., 2016***) as well as more nuanced strategies that flexibly use directional cues from different sensory modalities (***Wystrach et al., 2013***; ***Schwarz et al., 2017***; ***Dacke et al., 2019***). A priority of future works should be investigation of the differences and commonalities in sensory systems, neural structures and ecology of different insect navigators and how this impacts behaviour allowing for extension and refinement of the framework for different animals. Complimentary stress-testing of models across different environments in both simulation and robotic studies are also required to

ensure that model performance generalises across species and habitats and to provide guidance to researchers seeking the sensory, processing and learning circuits underpinning these abilities.

Methods and Materials

All source code related to this publication is available for download at https://github.com/XuelongSun/InsectNavigationToolkitModelling. All simulations and network models are implemented by Python 3.5 and make use of external libraries-*numpy*, *matplotlib*, *scipy*, *PIL* and *cv2*.

Simulated 3D world

The environment used in this study is that provided by ***Stone et al.*** (***2018***) which is itself adapted from ***Baddeley et al.*** (***2012***) (see ***Figure 6***C). It is a virtual ant-like world consisting of randomly generated bushes, trees and tussocks based on triangular patches (for more details see ***Baddeley et al.*** (***2012***)). Therefore, the data of this simulated world is stored in a matrix with the size of $N_P \times 3 \times 3$, defining the three dimensional coordinates (x,y,z) of the three vertices of N_P (number of patches) triangle patches. Agent movement was constrained to a $20m \times 20m$ training and test area allowing free movement without the requirement of an additional obstacle avoidance mechanism.

Image reconstruction

The agent's visual input at location (x, y) with the heading direction θ_h is simulated from a point 1cm above from the ground plane with field of view $360°$ wide by $90°$ high (centred on the horizon). This panoramic image (300×104) is then wrapped onto a sky-centred disk as required by the Zernike Moments transformation algorithm used with the size of $208(104 \times 2) \times 208$ ready for image processing (see ***Figure 6***D upper).

Image processing

Frequency encoding conceptual overview

Image compression algorithms such as JPEG encoding (***Hudson et al., 2018***) have long utilised the fact that a complex signal can be decomposed into a series of trigonometric functions that oscillate at different frequencies. The original signal can then be reconstructed by summing all (for prefect reconstruction) or some (for approximate reconstruction) of the base trigonometric functions. Thus, compression algorithms seek a balance between using the fewest trigonometric functions to encode the scene (for example, by omitting high frequencies that humans struggle to perceive), and the accuracy of the reconstructed signal (often given as an option when converting to JPEG format). ***Figure 6***A provides a cartoon of the frequency decomposition process for a panoramic view.

When such transforms are applied to fully panoramic images, or skylines, benefits beyond compression arise. Specifically, discrete transformation algorithms used to extract the frequency information generate a series of information triplets to describe the original function: frequency coefficients describe the frequency of the trigonometric function with associated **amplitudes** and *phase* values defining the vertical height versus the mean and the lateral position of the waveform respectively (***Figure 6***A). For panoramic views, regardless of the rotational angle of the image capturing device (eye or camera) the entire signal will always be visible and hence the **amplitudes** of the frequency coefficients do not alter with rotation (***Figure 6***B). This information has been used for successful place recognition in a series of robot studies (***Pajdla and Hlaváč, 1999***; ***Menegatti et al., 2004***; ***Stone et al., 2016***). Most recently (***Stone et al., 2018***) demonstrated that the difference between the **amplitudes** of the frequency coefficients recorded at two locations increases monotonically with distance producing an error surface suitable for visual homing. This feature of the frequency encoding underlies the visual homing results described in Mushroom bodies as drivers of rotational invariant visual homing.

In addition, as the *phase* of each coefficient describes how to align the signal this will naturally track any rotation in the panoramic view (***Figure 6***B) providing a means to realign with previous

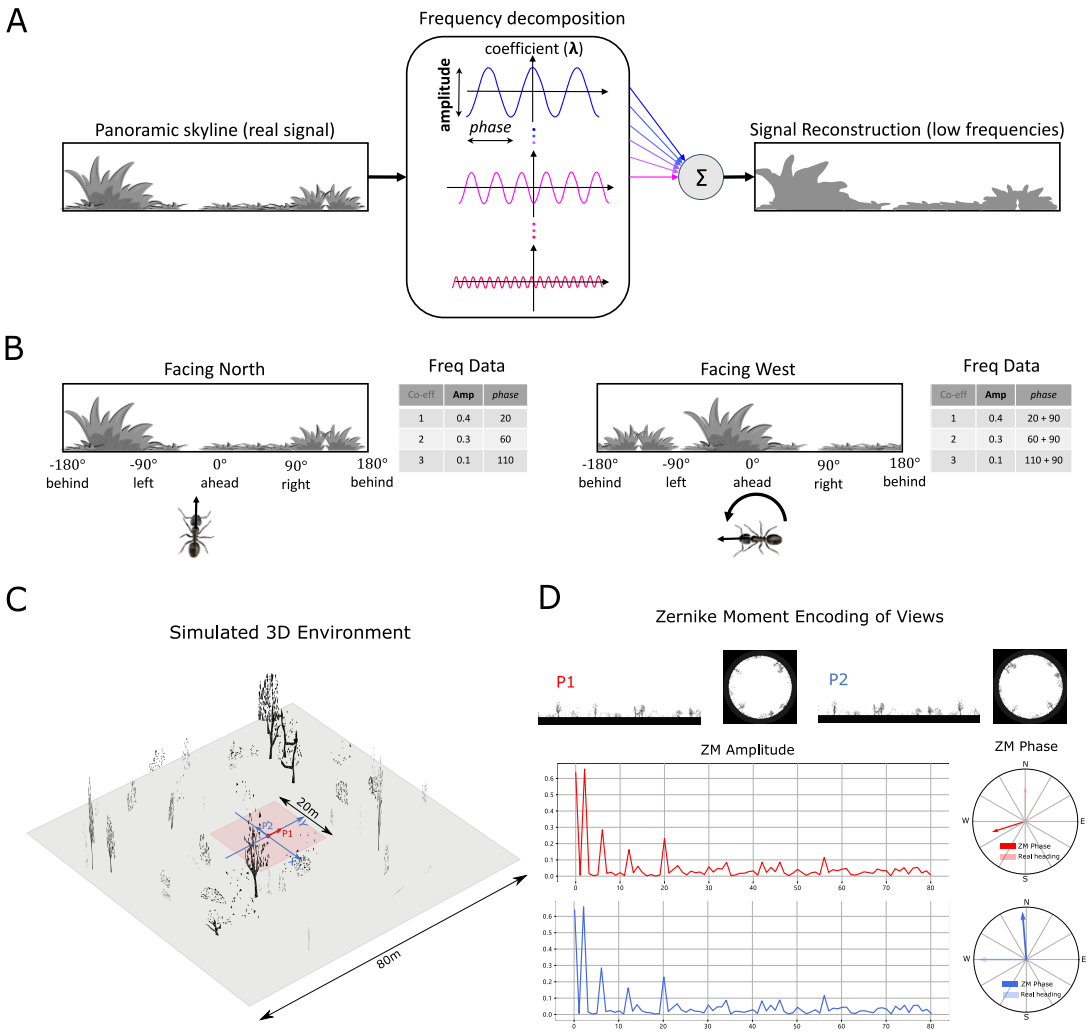

Figure 6. Information provided by frequency encoding in cartoon and simulated ant environments. (A): A cartoon depiction of a panoramic skyline, it's decomposition into trigonometric functions, and reconstruction through the summation of low frequency coefficients reflecting standard image compression techniques. **(B)**: Following a 90° rotation there is no change in the **amplitudes** of the frequency coefficients but the *phases* of the frequency coefficients track the change in orientation providing a rotational invariant signal useful for visual homing and rotationally-varying signal useful for route following respectively. **(C)**: The simulated 3D world used for all experiments. The pink area (size: $20m \times 20m$) is used for model training and testing zone for models allowing obstacle-free movement. **(D)**: The frequency encoding (Zernike Moment's **amplitudes** and *phase*) of the views sampled from the same location but with different headings (P1 and P2 in **(C)**, with $90°$ heading difference) in the simulated world. The first 81 **amplitudes** are identical while the *phases* have the difference of about $90°$.

Figure 6–source data 1. The matrix of simulated 3D world.

headings. The *phase* components of panoramic images have been utilised previously to derive the home direction in a visual homing task (***Stürzl and Mallot, 2006***). This feature of the frequency encoding underlies the route following results described in Route following in the insect brain.

The image processing field has created an array of algorithms for deriving the frequency content of continuous signals (***Jiang et al., 1996***; ***Gonzalez et al., 2004***). To allow exploration of the usefulness of frequency information, and how it could be used by the known neural structures, we adopt the same Zernike Moment algorithm used by ***Stone et al.*** (***2018***), but the reader should be clear that there are many alternate and more biologically plausible processes by which insects could derive similar information. It is beyond the scope of this proof of concept study to define

precisely how this process might happen in insects but future research possibilities are outlined in the Discussion.

Zernike Moments encoding

Zernike Moments (ZM) are defined as the projection of a function onto orthogonal basis polynomials called Zernike polynomials (***Teague, 1980***; ***Khotanzad and Hong, 1990***). This set of functions are defined on the unit circle with polar coordinates (ρ, θ) shown as:

$$V_{nm}(\rho, \theta) = R_{nm}(\rho)e^{jm\theta} \tag{1}$$

Where $n \in N^+$ is the order and m is the repetition meeting the condition: $m \in N$, $|m| \leq n$ and $n - |m|$ is even to ensure the rotational invariant property is met. $R_{nm}(\rho)$ is the radial polynomial defined as:

$$R_{nm}(\rho) = \sum_{s=0}^{n-|m|/2} (-1)^s \frac{(n-s)!}{s!(\frac{n+|m|}{2} - s)!(\frac{n-|m|}{2} - s)!} \rho^{n-2s} \tag{2}$$

For a continuous image function $f(x, y)$, the ZM coefficient can be calculated by:

$$Z_{nm}(\rho) = \frac{n+1}{\pi} \int\int_{x^2+y^2 \leq 1} f(x, y) V^*_{nm}(\rho, \theta) dx dy \tag{3}$$

For a digital image, summations can replace the integrals to give the ZM:

$$Z_{nm}(\rho) = \frac{n+1}{\pi} \sum_x \sum_y f(x, y) V^*_{nm}(\rho, \theta), \qquad x^2 + y^2 \leq 1. \tag{4}$$

ZM are extracted from the simulated insect views in wrapped format (***Figure 6***D) whose centre is taken to be the origin of the polar coordinates such that all valid pixels lie within the unit circle. For a given image I (P1 in ***Figure 6***D) and the rotated version of this image I^{θ_r} (P2 in ***Figure 6***D), the **amplitude** $A = |Z|$ and *phase* $\Phi = \angle Z$ of ZM coefficients of these two images will satisfy:

$$\begin{cases} |Z^{\theta_r}_{nm}| = |Z_{nm} e^{-jm\theta_r}| = |Z_{nm}| \quad i.e., \quad A^{\theta_r}_{nm} = A_{nm} \\ \Phi^{\theta_r}_{nm} = \Phi_{nm} - m\theta_r \end{cases} \tag{5}$$

From which we can see that the **amplitude** of the ZM coefficient remains the same while the *phase* of ZM carries the information regarding the rotation (see ***Figure 6***A and D). This property is the cornerstone of the visual navigation model where the **amplitudes** encode the features of the view while the *phase* defines the orientation.

Amplitudes for ZM orders ranging from $n = 0$ to $n = 16$ were selected as they appeared to cover the majority of information within the image. From ***Equation 1*** we know that $V_{n,m} = V_{n,-m}$, so we limited $m \in N^+$ to reduce the computational cost, which sets the total number of ZM coefficients (N_{ZM}) to $(16 \div 2 + 1)^2 = 81$ which was input to the visual navigation networks. For training the ANN network for RF, in ***Equation 5***, if we set $m = 1$, such that $\Phi^{\theta_r}_{n,1} = \Phi_{n,1} - \theta_r$ which means that all ZM coefficients will provide the same information when the image is rotated. Further, the difference between the *phase* of ZM coefficients of the current view with those of the memorised view, will inherently provide the angle with which to turn to realign oneself, i.e. :

$$\Phi^{current}_{7,1} - \Phi^{memory}_{7,1} = \theta_h - \theta_m \tag{6}$$

Where the order n of this ZM is selected to be $n = 7$ manually by comparing the performance with different orders in this specific virtual environment, θ_h is the current heading of the agent while θ_m is the memorised heading direction (desired heading direction).

Neural networks

We use the simple firing rate to model the neurons in the proposed networks, where the output firing rate C is a sigmoid function of the input I if there is no special note. In the following descriptions and formulas, a subscript is used to represent the layers or name of the neuron while the superscript is used to represent the value at a specific time or with a specific index.

Current headings

In the proposed model, there are two independent compass systems based on the global and the local cues respectively so named global and local compass correspondingly. These two compass systems have similar neural pathways from OL via AOTU and BU to the CX but ended distinct groupings of TB1 neurons: I-TB1 and II-TB1 in the PB.

Global compass

The global compass neural network applied in this study is the same as that of ***Stone et al.*** (***2017***), which has three layers of neurons: TL neurons, CL1 neurons and I-TB1 neurons. The 16 TL neurons respond to simulated polarised light input and are directly modelled as:

$$I_{TL} = \cos(\theta_{TL} - \theta_h) \tag{7}$$

Where $\theta_{TL} \in \{0, \pi/4, \pi/2, 3\pi/4, \pi, 5\pi/4, 3\pi/2, 7\pi/4\}$ is the angular preference of the 16 TL-neurons. The 16 CL1-neurons are inhibited by TL-neuron activity which invert the polarisation response:

$$I_{CL1} = 1.0 - C_{TL} \tag{8}$$

The 8 I-TB1 neurons act as a ring attractor creating a sinusoidal encoding of the current heading. Each I-TB1 neuron receives excitation from the CL1 neuron sharing the same directional preference and inhibition from other I-TB1 neurons via mutual connections:

$$W^{ij}_{I-TB1} = \frac{\cos(\theta^i_{I-TB1} - \theta^j_{I-TB1}) - 1}{2} \tag{9}$$

$$I^{t,j}_{I-TB1} = (1-c)C^{t,j}_{CL1} + c\sum_{i=1}^{8} W^{ij}_{I-TB1} C^{t-1,j}_{I-TB1} \tag{10}$$

Where c is a balance factor to modify the strength of the inhibition and the CL1 excitation. Finally, the population coding $C^{t,j}_{I-TB1}, j = 0, 1, ...7$ represents the heading of global compass of the agent at time t.

Local compass

The local compass is derived from the terrestrial cues through a similar visual pathway as the global compass and also ends in a ring attractor network. As for the global compass, the local compass heading is directly modelled by the population encoding of II-TB1 neurons:

$$C^i_{II-TB1} = \cos(\Phi_{7,1} - \theta^i_{II-TB1}) \qquad i = 0, 1, ...7 \tag{11}$$

Where θ_{II-TB1} is the angular preference of the II-TB1 neurons and $\Phi_{7,1}$ is the *phase* of ZM. Therefore, the firing rate of C_{II-TB1} encodes the heading of the local compass.

Visual homing

The neural network of visual homing is an associative network constrained by the anatomical structure of the mushroom body (MB) of the insects. In contrast to ***Ardin et al.*** (***2016***) where a spiking neural network is implemented to model the MB, we apply a simple version of MB where the average firing rates of neurons are used.

The visual projection neurons (vPNs) directly receive the **amplitudes** of the ZM coefficients as their firing rates:

$$C^i_{vPN} = A^i, \qquad i = 0, 1, 2...N_{vPN} \tag{12}$$

Where N_{vPN} is the number of the vPN neurons which is the same as the total number of ZM **amplitudes** applied and in this study $N_{vPN} = N_{ZM} = 81$. The A^i denotes the ith **amplitudes** of ZM coefficients.

The vPNs project into Kenyon cells (KC) through randomly generated binary connections W_{vPN2KC}, which result in the scenario wherein one KC receives 10 randomly selected vPNs' activation:

$$I_{KC}^{j} = \sum_{i=0}^{N_{vPN}} W_{vPN2KC}^{ji} C_{vPN}^{i} \tag{13}$$

Where I_{KC}^{j} denotes the total input current of jth KC from the vPN and the KCs are modelled as binary neurons with the same threshold Thr_{kc}:

$$C_{KC} = \begin{cases} 0 & if \quad I_{KC} \leq Thr_{KC} \\ 1 & if \quad I_{KC} > Thr_{KC} \end{cases} \tag{14}$$

The MBON neuron sums all the activation of Kenyon cells via plastic connections W_{KC2EN}:

$$C_{MBON} = \sum_{i=0}^{N_{KC}} W_{KC2MBON}^{i} C_{KC}^{i} \tag{15}$$

An anti-Hebbian learning rule is applied for the plasticity of $W_{KC2MBON}$ in a simple way:

$$W_{KC2MBON}^{t} = W_{KC2MBON}^{t-1} - \eta_{KC2MBON} \qquad if \quad C_{KC}^{i} \geq W_{KC2MBON}^{i} \tag{16}$$

Where $\eta_{KC2MBON}$ is the learning rate. The learning process will happen only when the reward signal is turned on. The activation of EN C_{MBON} represents the familiarity of the current view and the change of the C_{MBON} is defined as:

$$\Delta C_{MBON} = C_{MBON}^{t} - C_{MBON}^{t-1} \tag{17}$$

ΔC_{MBON} is used to track the gradient of the familiarity to guide the agent to the more familiar locations by shifting the I-TB1 neurons' activation C_{I-TB1}.

$$C_{VH}^{i} = C_{I-TB1}^{j}, j = \begin{cases} i + offset & if \quad i + offset \leq 7 \\ i + offset - 7 & otherwise \end{cases} \qquad i = 0, 1, ...7 \tag{18}$$

The relationship between the ΔC_{MBON} and the $offset$ is shown as following:

$$offset = \begin{cases} 0 & if \quad \Delta C_{MBON} < 0 \\ \min(\lfloor k_{VH} \Delta C_{MBON} \rfloor, 4) & otherwise \end{cases} \tag{19}$$

Path integration

The PI model implemented is that published by ***Stone et al.*** (***2017***). The core functionality arises from the CPU4 neurons that integrate the activation of TN2 neurons that encode the speed of the agent and the inverted activation of direction-sensitive I-TB1 neurons. The result is that the population of CPU4 neurons iteratively track the distance and orientation to the nest (a home vector) in a format akin to a series of directionally-locked odometers.

The firing rate of the CPU4 neurons are updated by:

$$I_{CPU4}^{t} = I_{CPU4}^{t-1} + r(C_{TN2}^{t} - C_{I-TB1}^{t} - k) \tag{20}$$

Where the rate of the memory accumulation $r = 0.0025$; the memory loss $k = 0.1$; the initial memory charge of CPU4 neurons $I_{CPU4}^{0} = 0.1$.

The input of the TN2 neurons encoding the speed is calculated by:

$$\begin{cases} I_{TN2_L} = [\sin(\theta_h + \theta_{TN2}) \cos(\theta_h + \theta_{TN2})]\boldsymbol{v} \\ I_{TN2_R} = [\sin(\theta_h - \theta_{TN2}) \cos(\theta_h - \theta_{TN2})]\boldsymbol{v} \end{cases} \tag{21}$$

where $\boldsymbol{v}$ is the velocity (see ***Equation 39***) of the agent and θ_{TN2} is the preference angle of the TN2 neurons. In this study $\theta_{TN2} = \pi/4$. The activation function applied to TN2 neurons is the rectified linear function given by:

$$C_{TN2} = \max(0, 2I_{TN2}) \tag{22}$$

As CPU4 neurons integrate the speed and direction of the agent, the desired heading of PI can be represented by the population encoding of these neurons, thus:

$$C_{PI} = C_{CPU4} \tag{23}$$

Route Following

The route following model is based on a simple artificial neural network (ANN) with just one hidden layer. The input layer directly takes the **amplitudes** of the ZM coefficients as the activation in the same way as that of visual projection neurons in MB network. This is a fully connected neural network with the sigmoid activation function, so the forward propagation is ruled by:

$$\begin{cases} Z_l^i = \sum_{i=0}^{N} W^{ji} Y_{l-1}^j \\ Y_i^l = sigmoid(Z_l^i) = \frac{1}{1+e^{-Z_l^i}} \end{cases} \quad i = 0, 1, ...7 \quad and \quad l = 0, 1, 2 \tag{24}$$

Where Z_l^i and Y_l^i denote the input and output of the ith neuron in l^{th} layer, thus the input is the same as the MB network $Z_0^i = A^i, i = 0, 1, ...N_{ZM}$ and the output of the ANN is consequently the population coding of the RF desired heading, i.e.:

$$C_{RF}^i = Y_i^2 \qquad i = 0, 1, ...7 \tag{25}$$

For a fast and efficient implementation, the learning method applied here is back propagation with gradient descend. Training data is derived from the **amplitudes** and the population encoded *phases* of the ZM coefficients of the images reconstructed along a habitual route. As shown in ***Equation 11*** the II-TB1 neurons encode the heading of local compass, therefore, the training pair for the RF network can be defined as $\{A, C_{II-TB1}\}$. After training, this network will correlate the desired ZM *phase* with the specific ZM **amplitudes**, and when RF is running, the output of this neural network C_{RF} will represent the desired heading with respect to the current heading of the local compass represented by the population encoding of II-TB1 neurons.

Coordination of elemental guidance strategies

The coordination of the three main navigation strategies PI, VH and RF are realised in distinct stages. Firstly, Off-route strategies (PI and VH) is optimally integrated by weighing according to the certainly of each before a context-dependent switch activates either On-route (RF) or Off-route strategies depending on the current visual novelty.

Optimal cue integration

A ring attractor neural network is used to integrate the cues from the VH and PI guidance systems. As reported in ***Hoinville and Wehner*** (***2018***) summation of directional cues represented in vector format leads to optimal angular cue integration which is the same case as real insects. ***Sun et al.*** (***2018***) gave a biology plausible way to do this kind of computation based on a simple ring attractor neural network. There are two populations of neurons in this network, the first is the integration neurons (IN) which is the output population of the network. Constrained by the number of columns in each hemisphere of the insects CX, we set the number of the IN to be 8, and its firing rate is updated by:

$$\tau \frac{dC_{IN}}{dt} = -C_{IN} + g\left(\sum_{j=1}^{n} W_{E2E}^{ji} C_{IN}^j + X_1^i + X_2^i + W_{I2E} C_{UI}\right) \qquad i = 0, 1, ...7. \tag{26}$$

Where W_{E2E}^{ji} is the recurrent connections from j^{th} neuron to i^{th} neuron, $g(x)$ is the activation function that provides the non-linear property of the neuron:

$$g(c) = max(0, \rho + c) \tag{27}$$

Where ρ denotes the offset of the function.

In ***Equation 26***, X_1 and X_2 generally denote the cues that should be integrated. In this study, X_1 and X_2 represent the desired heading of path integration (C_{PI}) and visual homing (C_{VH}). The desired heading of PI is also tuned by the tuning neuron (TUN) in SMP which is stimulated by the

MBON of MB (see ***Figure 3***A) and its activation function is defined by a rectified linear function, i.e.:

$$C_{TUN} = \min(k_{TUN} C_{EN}, 1) \tag{28}$$

Where k_{TUN} is the scaling factor.

Thus, the X_1 and X_2 for this ring attractor network can be calculated by:

$$\begin{cases} X_1^i = C_{TUN} C_{PI}^i \\ X_2^i = C_{VH}^i \end{cases} \qquad i = 0, 1, ...7 \tag{29}$$

The second population of the ring attractor is called the uniform inhibition (UI) neurons modelled by:

$$\tau \frac{dC_{UI}}{dt} = -u + g\left(W_{I2I} C_{UI} + W_{E2I} \sum_{k=1}^{n} C_{IN}^k\right) \qquad i = 0, 1, ...7. \tag{30}$$

After arriving at a stable state, the firing rate of the integration neurons in this ring attractor network provides the population encoding of the optimal integrated output C_{OI}:

$$C_{OI} = C_{CN} \tag{31}$$

Context-dependent switch

The model generates two current/desired headings pairs: the current heading of global compass decoded by C_{I-TB1} with the desired heading optimally integrated by the integration neurons of the ring attractor network C_{OI} and the current heading of local compass decoded by II-TB1 neurons C_{II-TB2} with the desired heading decoded by the output of the RF network C_{RF}. These two pairs of signal both are connected to the steering circuit (see ***Figure 5***A and Steering circuit) but are turned on/off by two switching neurons (SN1 and SN2) in the SMP (***Figure 5***A). SN2 neuron receives the activation from MBON neuron and is modelled as:

$$SN2 = \begin{cases} 0 & if \quad C_{MBON} < Thr_{SN2} \\ 1 & otherwise \end{cases} \tag{32}$$

While SN1 will always fire unless SN2 fires:

$$SN1 = \begin{cases} 0 & if \quad C_{SN2} = 1 \\ 1 & otherwise \end{cases} \tag{33}$$

Therefore, the context-depend switch is achieved according to the current visual novelty represented by the activation of MBON.

Steering circuit

The steering neurons, i.e., CPU1 neurons ($C_{CPU1}^i, i = 0, 1, 2...15$) receive excitatory input from the desired heading ($C_{DH}^i, i = 0, 1, 2...15$) and inhibitory input from the current heading ($C_{CH}, i = 0, 1, 2...15$) to generate the turning signal:

$$C_{ST}^i = C_{DH}^i - C_{CH}^i \qquad i = 0, 1, ...15 \tag{34}$$

The turning angle is determined by the difference of the activation summations between left ($i = 0, 1, 2...7$) and right ($i = 8, 9, 10...15$) set of CPU1 neurons:

$$\theta_M = k_{motor}\left(\sum_{i=0}^{7} C_{CPU1} - \sum_{i=8}^{15} C_{CPU1}\right) \tag{35}$$

which corresponds to the difference of the length of the subtracted left and right vectors in ***Figure 2***A. In addition, as it is illustrated in ***Figure 2***A, another key part of steering circuit is the left/right shifted desired heading, in this paper, this is achieved by the offset connectivity pattern ($W_{DH2CPU1L}$

and $W_{DH2CPU1R}$) from the desired heading to the steering neurons (***Heinze and Homberg, 2008***; ***Stone et al., 2017***):

$$\begin{cases} C_{DH}^{0-7} = C_{SN1}C_{RF}W_{DH2CPU1L} + C_{SN2}C_{OI}W_{DH2CPU1L} \\ C_{DH}^{8-15} = C_{SN1}C_{RF}W_{DH2CPU1R} + C_{SN2}C_{OI}W_{DH2CPU1R} \end{cases} \tag{36}$$

Where the $W_{DH2CPU1L}$ and $W_{DH2CPU1R}$ are:

$$W_{DH2CPU1L} = \begin{bmatrix} 0 & 1 & 0 & 0 & 0 & 0 & 0 & 0 \\ 0 & 0 & 1 & 0 & 0 & 0 & 0 & 0 \\ 0 & 0 & 0 & 1 & 0 & 0 & 0 & 0 \\ 0 & 0 & 0 & 0 & 1 & 0 & 0 & 0 \\ 0 & 0 & 0 & 0 & 0 & 1 & 0 & 0 \\ 0 & 0 & 0 & 0 & 0 & 0 & 1 & 0 \\ 0 & 0 & 0 & 0 & 0 & 0 & 0 & 1 \\ 1 & 0 & 0 & 0 & 0 & 0 & 0 & 0 \end{bmatrix} \quad W_{DH2CPU1R} = \begin{bmatrix} 0 & 0 & 0 & 0 & 0 & 0 & 0 & 1 \\ 0 & 1 & 0 & 0 & 0 & 0 & 0 & 0 \\ 0 & 0 & 1 & 0 & 0 & 0 & 0 & 0 \\ 0 & 0 & 0 & 1 & 0 & 0 & 0 & 0 \\ 0 & 0 & 0 & 0 & 1 & 0 & 0 & 0 \\ 0 & 0 & 0 & 0 & 0 & 1 & 0 & 0 \\ 0 & 0 & 0 & 0 & 0 & 0 & 1 & 0 \\ 0 & 0 & 0 & 0 & 0 & 0 & 0 & 1 \end{bmatrix} \tag{37}$$

which defines the connection pattern realising the left/right shifting of the desired headings used throughout our model ((***Figure 2***A, ***Figure 3***A, ***Figure 4***A, ***Figure 5***A and ***Figure 7***A).

The current heading input to the steering circuit is also switched between global and local compass input via the SN1 and SN2 neuron:

$$\begin{cases} C_{CH}^{0-7} = C_{SN1}C_{II-TB1} + C_{SN2}C_{I-TB1} \\ C_{CH}^{8-15} = C_{SN1}C_{II-TB1} + C_{SN2}C_{I-TB1} \end{cases} \tag{38}$$

Detailed neural connectivity of unified model

Figure 7A shows a complete picture of the proposed model. Specifically, it highlights the final coordination system showing that CX computing the optimal navigation output with the modulation from the MB and SMP. In addition, offset connectivity pattern from the desired heading to the steering circuit that underpin the left/right shifting is clearly shown. ***Figure 7***BC shows the network generating the desired heading of RF and VH respectively.

In addition, ***Table 1*** provides details of all modelled neural circuits with their function and naming conventions with links to biological evidence for these neural circuits where it exists and the animal that they were observed in.

Simulations

Equation 35 gives the turning angle of the agent, thus the instantaneous "velocity" ($\boldsymbol{v}$) at every step can be computed by:

$$\boldsymbol{v}^t = S_L[\cos\theta_M^t, \sin\theta_M^t] \tag{39}$$

Where S_L is the step length with the unit of centimetres. Note that we haven't defined the time accuracy for every step of the simulations, thus the unit of the velocity in this implementation is $cm/step$ rather than cm/s. Then the position of agent $\boldsymbol{P}^{t+1}$ in the Cartesian coordinates for the is updated by:

$$\boldsymbol{P}^{t+1} = \boldsymbol{P}^t + \boldsymbol{v}^t \tag{40}$$

The main parameter settings for all the simulations in this paper can be found in ***Table 2***.

Reproduce visual navigation behaviour

Inspired by the benchmark study of real ants in ***Wystrach et al.*** (***2012***), we test our model of VH and RF by reproducing the homing behaviours in that study. This is achieved by constructing a habitual route with a similar shape (arc or banana shape) in our simulated 3D world. The position $\boldsymbol{P}_{R-Arc}$ and heading θ_{R-Arc} along that route is manually generated by:

$$\begin{cases} \theta_{R-Arc}^i = \frac{\pi}{2} - i\frac{\pi}{2N_M} \\ \boldsymbol{P}_{R-Arc}^i = [-R\sin\theta_{R-Arc}^i, -7 + R\cos\theta_{R-Arc}^i] \end{cases} \quad i = 0, 1..N_M \tag{41}$$

Table 1. The details of the main neurons used in the proposed model

Name	Function	Num	Network	Brain region	Neuron in Species(e.g.)	Reference
I-TB1	Global compass current heading	8	Ring attractor	CX	TB1 in *Schistocerca gregaria* and *Megalopta genalis* Δ7 in *Drosophila*	***Heinze and Homberg*** (***2008***) ***Stone et al.*** (***2017***) ***Franconville et al.*** (***2018***)
II-TB1	Local compass current heading	8	Ring attractor			
S I-TB1	Copy of shifted global heading	8	Ring		No data	/
VH-L	VH desired heading left	8	Ring		No data	
VH-R	VH desired heading right	8	Ring		No data	
PI-L	PI desired heading left	8	Ring		CPU4 in *Schistocerca gregaria* and *Megalopta genalis* P-F3N2v in *Drosophila*	***Heinze and Homberg*** (***2008***) ***Stone et al.*** (***2017***) ***Franconville et al.*** (***2018***)
PI-R	PI desired heading right	8	Ring			
RF-L	RF desired heading left	8	Ring		No data	/
RF-R	RF desired heading right	8	Ring		No data	
RA-L	Cue integration left	8	Ring attractor		No data	
RA-R	Cue integration right	8	Ring attractor		No data	
CPU1	Comparing the current and desired heading	16	Steering circuit		CPU1 in *Schistocerca gregaria* and *Megalopta genalis* PF-LCre in *Drosophila*	***Heinze and Homberg*** (***2008***) ***Stone et al.*** (***2017***) ***Franconville et al.*** (***2018***)
vPN KCs MBON	visual projection Kenyon cells visual novelty	81 4000 1	Associative learning	MB	MB neurons in *Drosophila* *Camponotus* *Apis mellifera*	***Aso et al.*** (***2014***) ***Ehmer and Gronenberg*** (***2004***) ***Rybak and Menzel*** (***1993***)
TUN	Tuning weights from PI to RA	1	/	SMP	No data	/
SN1	Turn on/off the RF output to CPU1	1	Switch circuit		No data	
SN2	Turn on/off the RA output to CPU1	1	Switch circuit		No data	

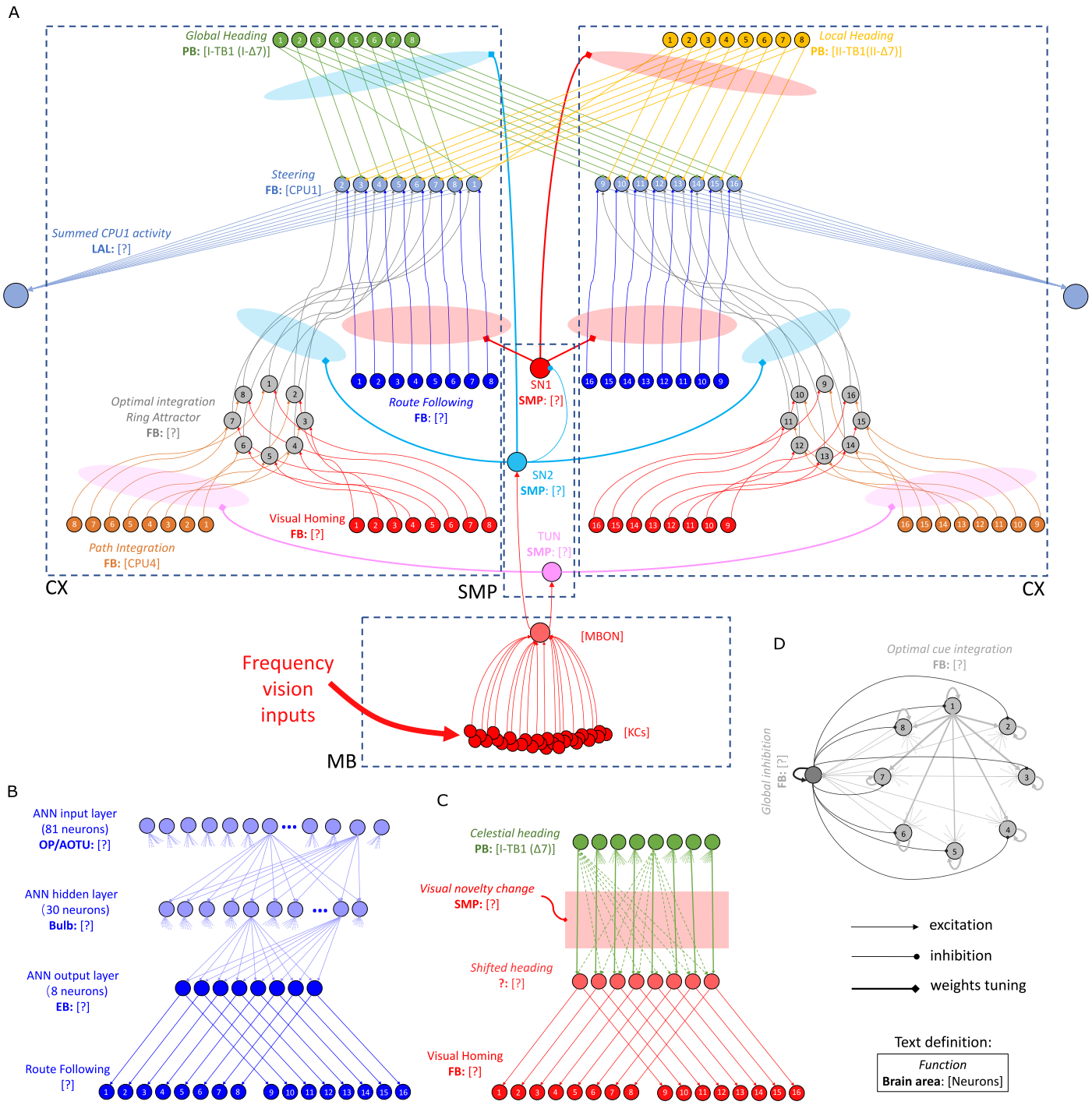

Figure 7. The detailed neural connections of the proposed model. (**A**): The detailed neural connections of the navigation coordination system. (**B**): The neural connection of the route following network. The input layer to the hidden layer is full connected, so does the hidden layer to the output layer. (**C**): The network generating the visual homing memory. (**D**): The detailed neural connection of the ring attractor network for optimal cue integration.

Where the $R = 7m$ is the radius of the arc and $N_M = 20$ in this case is the number of the sampling points where view images are reconstructed along the route. The reconstructed views then be wrapped and decomposed by ZM into **amplitudes** and *phases* are used to train the ANN network of RF and MB network of VH.

Table 2. The detailed parameters settings for the simulations

Para.	Visual Homing	Optimal Integration tuning PI	Optimal Integration tuning VH	Route Following	Whole model ZV	Whole model FV
Thr_{KC} (14)	0.04	0.04	0.04	0.04	0.04	0.04
$\eta_{KC2MBON}$ (16)	0.1	0.1	0.1	0.1	0.1	0.1
k_{VH} (19)	2.0	2.0	2.0	/	0.5	0.5
k_{TUN} (28)	/	0.1	0.1	/	0.025	0.0125
Thr_{SN2} (32)	/	/	/	/	2.0	3.0
k_{motor} (35)	0.125	0.125	0.125	0.125	0.375	0.375
S_L (cm/step) (39)	4	4	4	4	8	8
initial heading (deg)	0∼360	0∼360	0∼360	0 / 180	90	0

Visual homing

After training, 12 agents with different initial headings that were evenly distributed in $[0, 360)$ were released at the sideways release point ($\boldsymbol{P} = [0, -7]$) for the simulation of VH (***Figure 2***B). The headings of the agents at radius 2.5m from the release point (manually selected to ensure that the all the agents have completed any large initial loop) are taken as the initial headings.

Route following

After training, 2 agents with $0°$ and $180°$ are released at the different release points ($\boldsymbol{P} = [-9, -7]$, $[-8, -7], [-7, -7], [-6, -7], [-5, -7]$) for the simulation of RF (see ***Figure 4***B) to generate the homing path. And then, we release 12 agents on the route ($\boldsymbol{P} = [-7, -7]$) with different initial headings that is evenly distributed in $[0, 360)$ to compare the results with the real ant data in ***Wystrach et al.*** (***2012***). The heading of each agent at the position that is 0.6m from the release point is taken as the initial heading.

Reproduce the optimal cue integration behaviour

We evaluated the cue integration model by reproducing the results of ***Wystrach et al.*** (***2015***) and ***Legge et al.*** (***2014***). The ants' outbound routes in ***Wystrach et al.*** (***2015***) is bounded by the corridor, so here we simulate the velocity of the agent by:

$$\boldsymbol{v}_{out}^{t} = [rand(0, 2V_0) - V_0, V_0], \quad t = 0, 1...T_{out} \tag{42}$$

Where the function $rand(0, x)$ generates a random value from the uniform distribution of $[0, x]$, thus the speed of x-axis will be in $[-V_0, V_0]$ and will cancel each other during the forging. The speed of y-axis is constant so it will accumulated and be recorded by the PI model. And $V_0 = 1cm/step$ is the basic speed of the agent and T_{out} is the total time for outbound phase determining the length of the outbound route. As for the simulated homing route, we duplicate the outbound route when $T_{out} = 300$ but with a inverted heading direction. And then the visual navigation network was trained with images sampled along a simulated route (grey curve in ***Figure 3***B).

Tuning PI uncertainty

The agent in this simulation was allowed to forage to different distances of 0.1m, 1m, 3m or 7m from the nest to accrue different PI states and directional certainties before being translated to a never-before-experienced test site 1.5m from the nest. (RP1 in ***Figure 3***B). For each trial, we release 20 agents with different initial headings that is evenly distributed in $[0, 360)$. The headings of every agent at the position that is 0.6m from the start point is taken as the initial headings, and the mean direction and the 95% confidential intervals are calculated. As in the biological experiment, the angle between the directions recommended by the PI and visual navigation systems differed by approximately $130°$. As the length of the home vector increase (0.1m -> 7m) the activation of PI memory becomes higher (***Figure Supplement 1***B), and increasingly determines the output of the

ring attractor integration. Since the length of the home vector is also encoded in the activation of the PI memory neurons, the ring attractor can extract this information as the strength of the cue. As the visual familiarity is nearly the same in the vicinity of the release point, the strength of visual homing circuit remains constant and has more of an influence as the PI length drops.

Tuning visual uncertainty

The agent in this simulation was allowed to forage upto 1m from the nest to accrue its PI state and directional certainty before being translated to three different release points (RP1, RP2 and RP3 in ***Figure 3***B). As the distance from nest increases (RP1->RP2->RP3) so does the visual uncertainty. For each trial, we release 12 agents with different initial headings that is evenly distributed in $[0, 360)$. The headings of each agent at the position that is 0.3m from the start point is taken as the initial headings, and the mean direction and the 95% confidential intervals are calculated.

Whole model

The simulated habitual route is the same as in the simulation of visual navigation (Reproduce visual navigation behaviour) as is the learning learning procedure. The zero- and full- vector agents are both released at $[-2, -7]$ with the heading $0°$ and $90°$ respectively. The full-vector agent's PI memory is generated by letting the agent forage along the route from nest to feeder.

Acknowledgements

This research has received funding from the European Union's Horizon 2020 research and innovation programme under the Marie Sklodowska-Curie grant agreement No 778062, ULTRACEPT and No 691154, STEP2DYNA.

Thanks to the Barbara Webb and her Insects Robotics Research Team, Hadi Maboudi, Alex Cope and Andrew Philippedes for comments on early drafts, and to Antoine Wystrach for provision of data from previous works. Finally, thank you to our editor and reviewers who helped improve the model and manuscript through their excellent feedback.

References

Ardin P, Peng F, Mangan M, Lagogiannis K, Webb B. Using an Insect Mushroom Body Circuit to Encode Route Memory in Complex Natural Environments. PLoS Computational Biology. 2016; doi: 10.1371/journal.pcbi.1004683.

Aso Y, Hattori D, Yu Y, Johnston RM, Iyer NA, Ngo TTB, Dionne H, Abbott LF, Axel R, Tanimoto H, Rubin GM. The neuronal architecture of the mushroom body provides a logic for associative learning. eLife. 2014; 3:e04577. doi: 10.7554/eLife.04577.

Baddeley B, Graham P, Husbands P, Philippides A. A model of ant route navigation driven by scene familiarity. PLoS Computational Biology. 2012; doi: 10.1371/journal.pcbi.1002336.

Barth M, Heisenberg M. Vision affects mushroom bodies and central complex in Drosophila melanogaster. Learning & Memory. 1997; 4(2):219–229.

Beetz MJ, el Jundi B, Heinze S, Homberg U. Topographic organization and possible function of the posterior optic tubercles in the brain of the desert locust Schistocerca gregaria. Journal of Comparative Neurology. 2015; 523(11):1589–1607.

Bregy P, Sommer S, Wehner R. Nest-mark orientation versus vector navigation in desert ants. Journal of Experimental Biology. 2008; 211(12):1868–1873.

Cartwright B, Collett T. How honey bees use landmarks to guide their return to a food source. Nature. 1982; 295(5850):560.

Collett M. How navigational guidance systems are combined in a desert ant. Current Biology. 2012; 22(10):927–932.

Collett M, Chittka L, Collett TS. Spatial memory in insect navigation. Current Biology. 2013; 23(17):R789–R800. http://dx.doi.org/10.1016/j.cub.2013.07.020, doi: 10.1016/j.cub.2013.07.020.

Collett M, Collett TS. How does the insect central complex use mushroom body output for steering? Current Biology. 2018; 28(13):R733–R734. http://dx.doi.org/10.1016/j.cub.2018.05.060, doi: 10.1016/j.cub.2018.05.060.

Collett TS. Path integration: how details of the honeybee waggle dance and the foraging strategies of desert ants might help in understanding its mechanisms. Journal of Experimental Biology. 2019; 222(11):jeb205187.

Collett T. Insect navigation en route to the goal: multiple strategies for the use of landmarks. Journal of Experimental Biology. 1996; 199(1):227–235.

Cruse H, Wehner R. No need for a cognitive map: decentralized memory for insect navigation. PLoS computational biology. 2011; 7(3):e1002009.

Dacke M, Bell AT, Foster JJ, Baird EJ, Strube-Bloss MF, Byrne MJ, el Jundi B. Multimodal cue integration in the dung beetle compass. Proceedings of the National Academy of Sciences. 2019; p. 201904308.

Dewar ADM, Philippides A, Graham P. What is the relationship between visual environment and the form of ant learning-walks? An in silico investigation of insect navigation. Adaptive Behavior. 2014; 22(3):163–179. https://doi.org/10.1177/1059712313516132, doi: 10.1177/1059712313516132.

Ehmer B, Gronenberg W. Segregation of visual input to the mushroom bodies in the honeybee (Apis mellifera). Journal of Comparative Neurology. 2002; 451(4):362–373.

Ehmer B, Gronenberg W. Mushroom body volumes and visual interneurons in ants: comparison between sexes and castes. Journal of Comparative Neurology. 2004; 469(2):198–213.

El Jundi B, Foster JJ, Khaldy L, Byrne MJ, Dacke M, Baird E. A snapshot-based mechanism for celestial orientation. Current biology. 2016; 26(11):1456–1462.

Fisher YE, Lu J, D'Alessandro I, Wilson RI. Sensorimotor experience remaps visual input to a heading-direction network. Nature. 2019; 576(7785):121–125.

Fleischmann PN, Christian M, Müller VL, Rössler W, Wehner R. Ontogeny of learning walks and the acquisition of landmark information in desert ants, Cataglyphis fortis. Journal of Experimental Biology. 2016; 219(19):3137–3145.

Franconville R, Beron C, Jayaraman V. Building a functional connectome of the Drosophila central complex. eLife. 2018; 7. doi: 10.7554/elife.37017.

Fukushi T, Wehner R. Navigation in wood ants Formica japonica: context dependent use of landmarks. Journal of Experimental Biology. 2004; 207(19):3431–3439.

Gkanias E, Risse B, Mangan M, Webb B. From skylight input to behavioural output: a computational model of the insect polarised light compass. PLoS computational biology. 2019; 15(7):e1007123.

Gonzalez RC, Woods RE, Eddins SL. Digital image processing using MATLAB. Pearson Education India; 2004.

Graham P, Philippides A, Baddeley B. Animal cognition: multi-modal interactions in ant learning. Current Biology. 2010; 20(15):R639–R640.

Green J, Adachi A, Shah KK, Hirokawa JD, Magani PS, Maimon G. A neural circuit architecture for angular integration in Drosophila. Nature. 2017; 546(7656):101.

Gronenberg W, López-Riquelme G. Multisensory convergence in the mushroom bodies of ants and bees. Acta Biologica Hungarica. 2004; 55(1-4):31–37.

Harrison JF, Fewell JH, Stiller TM, Breed MD. Effects of experience on use of orientation cues in the giant tropical ant. Animal behaviour. 1989; .

Hausen K, Egelhaaf M. Neural mechanisms of visual course control in insects. In: *Facets of vision* Springer; 1989.p. 391–424.

Heinze S. Unraveling the neural basis of insect navigation. Current Opinion in Insect Science. 2017; 24(Figure 1):58–67. http://dx.doi.org/10.1016/j.cois.2017.09.001, doi: 10.1016/j.cois.2017.09.001.

Heinze S, Homberg U. Maplike representation of celestial E-vector orientations in the brain of an insect. Science. 2007; 315(5814):995–997.

Heinze S, Homberg U. Neuroarchitecture of the central complex of the desert locust: Intrinsic and columnar neurons. Journal of Comparative Neurology. 2008; 511(4):454–478. doi: 10.1002/cne.21842.

Heinze S, Homberg U. Linking the input to the output: new sets of neurons complement the polarization vision network in the locust central complex. Journal of Neuroscience. 2009; 29(15):4911–4921.

Heinze S, Narendra A, Cheung A. Principles of Insect Path Integration. Current Biology. 2018; 28(17):R1043–R1058. https://doi.org/10.1016/j.cub.2018.04.058, doi: 10.1016/j.cub.2018.04.058.

Heinze S, Pfeiffer K. The insect central complex-from sensory coding to directing movement. Frontiers in behavioral neuroscience. 2018; 12:156.

Heisenberg M. Mushroom body memoir: from maps to models. Nature Reviews Neuroscience. 2003; 4(4):266.

Hoinville T, Wehner R. Optimal multiguidance integration in insect navigation. Proceedings of the National Academy of Sciences. 2018; 115(11):201721668. http://www.pnas.org/lookup/doi/10.1073/pnas.1721668115, doi: 10.1073/pnas.1721668115.

Hoinville T, Wehner R, Cruse H. Learning and retrieval of memory elements in a navigation task. In: *Conference on Biomimetic and Biohybrid Systems* Springer; 2012. p. 120–131.

Homberg U, Hofer S, Pfeiffer K, Gebhardt S. Organization and neural connections of the anterior optic tubercle in the brain of the locust, Schistocerca gregaria. Journal of Comparative Neurology. 2003; 462(4):415–430.

Honkanen A, Adden A, da Silva Freitas J, Heinze S. The insect central complex and the neural basis of navigational strategies. The Journal of Experimental Biology. 2019; 222(Suppl 1):jeb188854. doi: 10.1242/jeb.188854.

Horridge GA. Pattern discrimination by the honeybee: disruption as a cue. Journal of Comparative Physiology A. 1997; 181(3):267–277.

Hudson G, Léger A, Niss B, Sebestyén I, Vaaben J. JPEG-1 standard 25 years: past, present, and future reasons for a success. Journal of Electronic Imaging. 2018; 27(4):040901.

James A, Osorio D. Characterisation of columnar neurons and visual signal processing in the medulla of the locust optic lobe by system identification techniques. Journal of Comparative Physiology A. 1996; 178(2):183–199.

Jeffery KJ, Page HJ, Stringer SM. Optimal cue combination and landmark-stability learning in the head direction system. The Journal of physiology. 2016; 594(22):6527–6534.

Jiang H, Paulsen KD, Osterberg UL, Pogue BW, Patterson MS. Optical image reconstruction using frequency-domain data: simulations and experiments. JOSA A. 1996; 13(2):253–266.

Khotanzad A, Hong YH. Invariant image recognition by Zernike moments. IEEE Transactions on pattern analysis and machine intelligence. 1990; 12(5):489–497.

Kim IS, Dickinson MH. Idiothetic path integration in the fruit fly Drosophila melanogaster. Current Biology. 2017; 27(15):2227–2238.

Kim SS, Hermundstad AM, Romani S, Abbott L, Jayaraman V. Generation of stable heading representations in diverse visual scenes. Nature. 2019; 576(7785):126–131.

Kodzhabashev A, Mangan M. Route following without scanning. In: *Conference on Biomimetic and Biohybrid Systems* Springer; 2015. p. 199–210.

Kohler M, Wehner R. Idiosyncratic route-based memories in desert ants, Melophorus bagoti: how do they interact with path-integration vectors? Neurobiology of learning and memory. 2005; 83(1):1–12.

Legge ELG, Wystrach A, Spetch ML, Cheng K. Combining sky and earth: desert ants (Melophorus bagoti) show weighted integration of celestial and terrestrial cues. Journal of Experimental Biology. 2014; 217(23):4159–4166. http://jeb.biologists.org/cgi/doi/10.1242/jeb.107862, doi: 10.1242/jeb.107862.

Lehrer M. Shape perception in the honeybee: symmetry as a global framework. International Journal of Plant Sciences. 1999; 160(S6):S51–S65.

Mangan M, Webb B. Spontaneous formation of multiple routes in individual desert ants (Cataglyphis velox). Behavioral Ecology. 2012; 23(5):944–954. doi: 10.1093/beheco/ars051.

Menegatti E, Maeda T, Ishiguro H. Image-based memory for robot navigation using properties of omnidirectional images. Robotics and Autonomous Systems. 2004; 47(4):251–267.

Müller J, Nawrot M, Menzel R, Landgraf T. A neural network model for familiarity and context learning during honeybee foraging flights. Biological cybernetics. 2018; 112(1-2):113–126.

Müller M, Wehner R. Path integration provides a scaffold for landmark learning in desert ants. Current Biology. 2010; 20(15):1368–1371.

Narendra A. Homing strategies of the Australian desert ant Melophorus bagoti II. Interaction of the path integrator with visual cue information. Journal of Experimental Biology. 2007; 210(10):1804–1812.

O'Carroll D. Feature-detecting neurons in dragonflies. Nature. 1993; 362(6420):541.

Ofstad TA, Zuker CS, Reiser MB. Visual place learning in Drosophila melanogaster. Nature. 2011; 474. doi: 10.1038/nature10131.

Omoto JJ, Keleş MF, Nguyen BCM, Bolanos C, Lovick JK, Frye MA, Hartenstein V. Visual input to the Drosophila central complex by developmentally and functionally distinct neuronal populations. Current Biology. 2017; 27(8):1098–1110.

Pajdla T, Hlaváč V. Zero phase representation of panoramic images for image based localization. In: *International Conference on Computer Analysis of Images and Patterns* Springer; 1999. p. 550–557.

Paulk AC, Kirszenblat L, Zhou Y, van Swinderen B. Closed-loop behavioral control increases coherence in the fly brain. Journal of Neuroscience. 2015; 35(28):10304–10315.

Pfeiffer K, Homberg U. Organization and functional roles of the central complex in the insect brain. Annual review of entomology. 2014; 59:165–184.

Plath JA, Entler BV, Kirkerud NH, Schlegel U, Galizia CG, Barron AB. Different Roles for Honey Bee Mushroom Bodies and Central Complex in Visual Learning of Colored Lights in an Aversive Conditioning Assay. Frontiers in Behavioral Neuroscience. 2017; 11(May). doi: 10.3389/fnbeh.2017.00098.

Reppert SM, Guerra PA, Merlin C. Neurobiology of monarch butterfly migration. Annual review of entomology. 2016; 61.

Rybak J, Menzel R. Anatomy of the mushroom bodies in the honey bee brain: the neuronal connections of the alpha-lobe. Journal of Comparative Neurology. 1993; 334(3):444–465.

Schwarz S, Mangan M, Zeil J, Webb B, Wystrach A. How ants use vision when homing backward. Current Biology. 2017; 27(3):401–407.

Seelig JD, Jayaraman V. Feature detection and orientation tuning in the Drosophila central complex. Nature. 2013; 503(7475):262–266. http://dx.doi.org/10.1038/nature12601, doi: 10.1038/nature12601.

Seelig JD, Jayaraman V. Neural dynamics for landmark orientation and angular path integration. Nature. 2015; 521(7551):186–191. doi: 10.1038/nature14446.

Steinbeck F, Adden A, Graham P. Connecting brain to behaviour: a role for general purpose steering circuits in insect orientation? Journal of Experimental Biology. 2020; 223(5).

Stone T, Differt D, Milford M, Webb B. Skyline-based localisation for aggressively manoeuvring robots using UV sensors and spherical harmonics. In: *2016 IEEE International Conference on Robotics and Automation (ICRA)* IEEE; 2016. p. 5615–5622.

Stone T, Mangan M, Wystrach A, Webb B. Rotation invariant visual processing for spatial memory in insects. Interface Focus. 2018; doi: 10.1098/rsfs.2018.0010.

Stone T, Webb B, Adden A, Weddig NB, Honkanen A, Templin R, Wcislo W, Scimeca L, Warrant E, Heinze S. An Anatomically Constrained Model for Path Integration in the Bee Brain. Current Biology. 2017; 27(20):3069–3085.e11. https://doi.org/10.1016/j.cub.2017.08.052, doi: 10.1016/j.cub.2017.08.052.

Stürzl W, Mallot HA. Efficient visual homing based on Fourier transformed panoramic images. Robotics and Autonomous Systems. 2006; 54(4):300–313.

Stürzl W, Zeil J, Boeddeker N, Hemmi JM. How wasps acquire and use views for homing. Current Biology. 2016; 26(4):470–482.

Sun X, Mangan M, Yue S. An analysis of a ring attractor model for cue integration. In: *Conference on Biomimetic and Biohybrid Systems* Springer; 2018. p. 459–470.

Teague MR. Image analysis via the general theory of moments. JOSA. 1980; 70(8):920–930.

Touretzky DS. Attractor network models of head direction cells. Head direction cells and the neural mechanisms of spatial orientation. 2005; p. 411–432.

Webb B. The internal maps of insects. The Journal of Experimental Biology. 2019; 222(Suppl 1):jeb188094. doi: 10.1242/jeb.188094.

Wehner R. The architecture of the desert ant's navigational toolkit. Myrmecological News. 2009; 12(September):85–96.

Wystrach A, Beugnon G, Cheng K. Ants might use different view-matching strategies on and off the route. Journal of Experimental Biology. 2012; 215(1):44–55. http://jeb.biologists.org/cgi/doi/10.1242/jeb.059584, doi: 10.1242/jeb.059584.

Wystrach A, Mangan M, Philippides A, Graham P. Snapshots in ants? New interpretations of paradigmatic experiments. Journal of Experimental Biology. 2013; 216(10):1766–1770. doi: 10.1242/jeb.082941.

Wystrach A, Beugnon G, Cheng K. Landmarks or panoramas: what do navigating ants attend to for guidance? Frontiers in Zoology. 2011; 8(1):21.

Wystrach A, Lagogiannis K, Webb B. Continuous lateral oscillations as a core mechanism for taxis in drosophila larvae. eLife. 2016; 5(OCTOBER2016). doi: 10.7554/eLife.15504.

Wystrach A, Mangan M, Webb B. Optimal cue integration in ants. Proceedings of the Royal Society B: Biological Sciences. 2015; 282(1816). doi: 10.1098/rspb.2015.1484.

Xu CS, Januszewski M, Lu Z, Takemura Sy, Hayworth K, Huang G, Shinomiya K, Maitin-Shepard J, Ackerman D, Berg S, et al. A connectome of the adult drosophila central brain. BioRxiv. 2020; .

Yilmaz A, Grübel K, Spaethe J, Rössler W. Distributed plasticity in ant visual pathways following colour learning. Proceedings of the Royal Society B. 2019; 286(1896):20182813.

Zeil J. Visual homing: an insect perspective. Current opinion in neurobiology. 2012; 22(2):285–293.

Zeil J, Fleischmann PN. The learning walks of ants (Hymenoptera: Formicidae). Myrmecological News. 2019; 29.

Zeil J, Hofmann MI, Chahl JS. Catchment areas of panoramic snapshots in outdoor scenes. JOSA A. 2003; 20(3):450–469.

Zeil J, Kelber A, Voss R. Structure and function of learning flights in ground-nesting bees and wasps. Journal of Experimental Biology. 1996; 199(1):245–252.

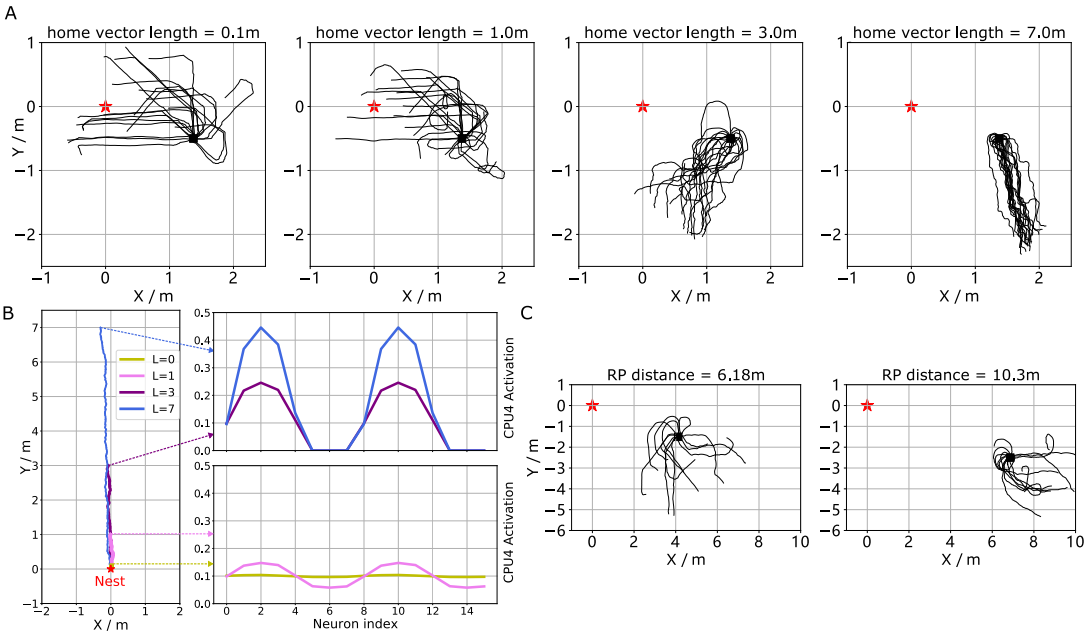

Figure 3–Figure supplement 1. The extended homing paths and the PI memory in the simulations. **(A)** The extended homing path of 20 agents released at RP1 in Figure 3B with different home vector length. **(B)** The activation of CPU4 neurons (PI memory) encoding home vectors with different lengths from 0 to 7.0m. **(C)** The extended homing paths of 20 agents released at RP2 and RP3 in Figure 3B.